

Zircon from the East Orebody of the Bayan Obo Fe–Nb–REE deposit, China, and SHRIMP ages for carbonatite-related magmatism and REE mineralization events

L. S. Campbell · W. Compston · K. N. Sircombe ·
C. C. Wilkinson

Received: 15 June 2013 / Accepted: 7 July 2014 / Published online: 8 August 2014
© The Author(s) 2014. This article is published with open access at Springerlink.com

Abstract Extremely U-depleted (<1 ppm) zircons from H8 banded ores in the East Orebody of the Bayan Obo REE–Nb–Fe deposit are presented, with mineral compositions, textures, ^{232}Th – ^{208}Pb SHRIMP ages and petrological context. Cores of East Orebody zircon contain up to 7 wt% HfO_2 and are zoned, depicting bipyramidal crystal forms. A distinct generation of patchy, epitaxial rim zircon, similarly depleted in U, is intergrown with rare earth ore minerals (bastnäsite, parisite, monazite). Overprinting aegirine textures indicate paragenetically late, reactive Na-rich fluids. Chondrite-normalized REE patterns without Eu anomalies

match closely with those from the Mud Tank and Kovdor carbonatitic zircons. Increased HREE in rims ((Lu/Gd)_N 43–112) relative to cores ((Lu/Gd)_N 6–7.5) and the localized presence of xenotime are attributable to reactive, mineralizing fluid compositions enriched in Y, REE and P. Cathodoluminescence further reveals HREE fractionation in rims, evidenced by a narrow-band Er^{3+} emission at 405 nm. The extreme depletion of U in core and rim zircon is characteristic for this mineral deposit and is indicative of a persistent common source. U depletion is also a characteristic for zircons from carbonatitic or kimberlitic systems. ^{232}Th – ^{208}Pb (SHRIMP II) geochronological data reveal the age of zircon cores as $1,325 \pm 60$ Ma and a rim-alteration event as 455.6 ± 28.27 Ma. The combined findings are consistent with a protolithic igneous origin for zircon cores, from a period of intrusive, alkaline–carbonatitic magmatism. Fluid processes responsible for the REE–Nb mineralizations affected zircon rim growth and degradation during the widely reported Caledonian events, providing a new example in a localized context of HREE enrichment processes.

Communicated by Jon Blundy.

Electronic supplementary material The online version of this article (doi:10.1007/s00410-014-1041-3) contains supplementary material, which is available to authorized users.

L. S. Campbell (✉)
School of Earth, Atmospheric and Environmental Sciences,
University of Manchester, Williamson Building, Oxford Road,
Manchester M13 9PL, UK
e-mail: Linda.Campbell@manchester.ac.uk

W. Compston
Research School of Earth Sciences, Australian National
University, Canberra, ACT 0200, Australia

K. N. Sircombe
Minerals Division, Geoscience Australia, Canberra, ACT 2609,
Australia

C. C. Wilkinson
Department of Earth Science and Engineering, Imperial
College London, South Kensington Campus, Exhibition Road,
London SW7 2AZ, UK

C. C. Wilkinson
Department of Earth Sciences, Natural History Museum,
Cromwell Road, London SW7 5BD, UK

Keywords Zircon · SHRIMP geochronology · Rare earth elements · HREE fractionation · Cathodoluminescence spectroscopy · Carbonatites

Introduction

The Bayan Obo Fe–Nb–REE-ore deposit was first known in the early twentieth century only for its iron-ore reserves, mainly magnetite with some haematite. It was only later that the high concentrations of rare earth ore minerals and niobium were recognized, and today it is the largest REE deposit known, accounting for much of China's domination

of world production of rare earth oxides (Chakhmouradian and Wall 2012; Hatch 2012). Yet the origin of the deposit is still under much discussion (Kynicky et al. 2012, and Smith et al. 2014). Situated within deformed sheets of a succession of Proterozoic metasediments known as the Bayan Obo Group in the North China Craton, and considered no younger than about ~1,200–1,400 Ma (Drew et al. 1990; Chao et al. 1997; Yang et al. 2011a, b), the host rock to the Fe–Nb–REE orebodies is known as “H8 Dolomite” in the published geological map of Drew and Meng (1990). Mineralogy of the unaltered unit is indicated by Drew et al. (1990) as a simple assemblage of sedimentary calcite and dolomite, but in the orebodies area, a much more diverse mineralogy is found, which, in highly varying proportions, can include alkali silicates (riebeckite, albite, aegirine, phlogopite), monazite, magnetite, apatite, fluorite, calcite, dolomite, baryte and rare earth fluorocarbonates (Smith et al. 2014). The main outcrop of H8 is up to 1×18 km and aligned ENE/WSW, along with sets of thrust faults with a similar trend (Drew and Meng 1990; Drew et al. 1990). In the hybrid map/satellite image of Fig. 1a, some extensive ribbons of stockpile can be seen which limit accessibility and mask, in particular, the exposure of the northern contact of the H8 dolomite. The succession is best shown in Tao et al., (1998), Fan et al. (2006), and in Yang et al. (2011a) along with the locations of some carbonatite dykes in the region. Yang and Woolley (2006) affirm the recent recognition of H9 (previously described as slate), as metamorphosed trachyte and basalt, with reference to the work of Hao et al. (2002). Other authors have also reported alkaline igneous rocks in the region of a variety of ages since about ~1.9 Ga (e.g. Nie et al. 2002 reporting 302–249 Ma, and Wang et al. 2003 reporting 1.54–1.92 Ga) refreshing the question of the placement of the deposit among the more unusual categories of “carbonatite clans” as explained by Mitchell (2005).

Small carbonatite dykes (1–2 m thick) intrude various parts of the Bayan Obo Group within a few km of the orebodies (Drew et al. 1990; Tao et al. 1998; Le Bas et al. 1992; Yang et al. 2003; Yang and Woolley 2006; Le Bas et al. 2007) and are dated at $1,354 \pm 59$ (Yang et al. 2011a). Zircons in three carbonatite dykes in the Bayan Obo region yield dates of 1,894–1,956 Ma and unremarkable Th/U ratios, and they contain inclusions of quartz and feldspar, features which are consistent with basement inheritance as reported by Liu et al. (2008) (see Table 1). In Yang et al. (2011b), $1,227 \pm 60$ Ma mafic dykes together with $1,354 \pm 59$ Ma carbonatite dykes are associated with marginal rifting that occurred during the break-up of the supercontinent Columbia and thought to be a part of extensive global magmatism events in the Mesoproterozoic (Ernst et al. 2008). A substantial diversity of ages of alkaline–carbonatite magmatic events is consistent with

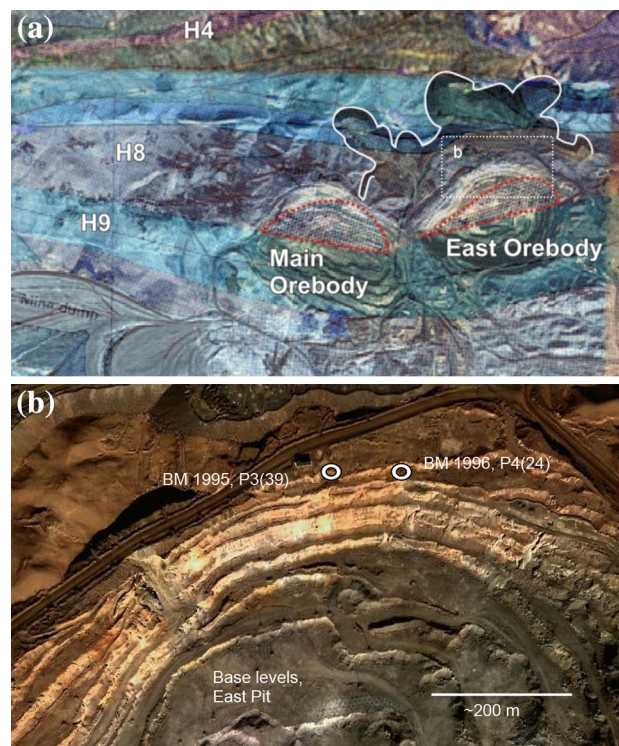


Fig. 1 Bayan Obo location **a** geological map (Drew and Meng 1990) superimposed onto a terrain image (Google Earth) of the 4×2.5 km study area, centred on $41^{\circ}48'12$ N and $109^{\circ}57'50$ E. The Main and East orebodies are outlined in *orange dash* and the northern mine dump area, obscuring much of the northern boundary of H8, is partially outlined in *white*. The Google Earth source consisted of a mosaic of images from the Landsat ETM+ (30 m spatial resolution) and Quickbird (60 cm resolution) for two different dates. The Quickbird data covered the main pits. The image was clipped from Google Earth and geometrically registered to the original UTM (WGS84) coordinate system using ground control points extracted from Google Earth. The geological map was scanned at a resolution of 600 dpi, converted to jpeg format and geometrically corrected using ten ground control points also determined from features in the Google Earth imagery. Data processing was carried out using the Erdas Imagine image processing software. This software was also used for data visualization including image overlays and the application of blending to allow visualization of map and terrain. **b** Terrain image of the northern section of the East Pit showing approximate locations of samples (collected on two separate field visits in 1990 and 1995) from the northern part of the 1,582 m level

other carbonatitic provinces globally, as shown in the world carbonatites map of Woolley and Kjarsgaard (2008) in which it can be seen that carbonatite occurrences tend to be location specific and age diverse, thus providing strong evidence for lithospheric origins for the source magmas (Woolley and Bailey 2012).

A wide envelope of fenitizing mineralizations, often characterized by overprinting alkali silicates, is now well documented for the Bayan Obo deposit (e.g. Yuan et al. 2000; Smith 2007; Le Bas 2008). This is consistent with a general consensus that a diverse set of mineralizing fluids

Table 1 Brief overview of Bayan Obo geochronology

Material	Method	Age (Ma)	Reference
Whole rock	Sm–Nd	1,580	Yuan et al. (1992)
Whole rock (trachytic)	Sm–Nd	1,096	Yuan et al. (2000)
Whole rock (H8/orebodies area)	Sm–Nd	1,273 ± 100	Zhang et al.(2001)
Whole rock (H8/orebodies area)	Sm–Nd	1,341 ± 160	Yang et al. (2011a)
Whole rock (H9 “K-slates”)	Sm–Nd	1,096 ± 56	Zhang et al.(2001)
Whole rock (H9 “dark-slates”)	Sm–Nd	1,208 ± 123	Zhang et al.(2001)
Bastnäsite and monazite (main Orebody)	Sm–Nd	1,313 ± 41	Zhang et al.(2001)
Whole rock (carbonatite dykes)	Sm–Nd	1,354 ± 59	Yang et al. (2011a)
Kuangu carbonatite vein	Rb–Sr	433	Yuan et al. (1992)
Aeschynite	²³² Th– ²⁰⁸ Pb	273	“Other workers” quoted by Yuan et al. (1992)
Biotite	Rb–Sr	255	“Other workers” quoted by Yuan et al. (1992)
Bastnäsite and monazite	²³² Th– ²⁰⁸ Pb	532–418	Chao et al. (1992)
Monazite	²³² Th– ²⁰⁸ Pb	555–398	Wang et al. (1994)
REE minerals (excluding monazite) and aegirine	¹⁴⁷ Sm– ¹⁴³ Nd	425	Wang et al. (1994)
Zircon in quartz-monzonite, Hejao, ~50 km to south	U–Pb	451 ± 17	Wang et al. (1994)
Zircon in anorogenic magmatic rocks	U–Pb	1,800	Wang et al. (2003)
Zircon in carbonatite dykes (inherited basement)	U–Pb	1,894–1,956	Liu et al. (2008)
Zircon in basement gneiss	U–Pb	1,917–1,948	Wang et al. (2002)
East Orebody zircon CORES	²³² Th– ²⁰⁸ Pb	1,325 ± 60 Ma	This paper
East Orebody zircon RIMS	²³² Th– ²⁰⁸ Pb	455.6 ± 28.3	This paper

evolved at Bayan Obo, with compositions closely associated with alkaline–carbonatite suites (Campbell and Henderson 1997; Smith et al. 1999, 2000; Smith and Henderson 2000; Yuan et al. 2000; Zhang et al. 2003; Wang et al. 2003; Fan et al. 2004; Ni et al. 2004; Fan et al. 2006; Smith 2007; Kynicky et al. 2012; Smith and Spratt 2012; Smith et al. 2014). A current review of the geochemical and isotopic complexity of Bayan Obo is explained in Smith et al. (2014), culminating with an overall genetic model for the deposit, and highlighting key remaining questions. Controls on rare earth mineralizations generally, and specifically for Bayan Obo, are best understood with reference to a thematic volume on rare earths (Chakhmouradian and Wall 2012).

Zircon and xenotime of the present study were first reported by Campbell (1998) and represent the only known occurrence of zircon from either the Main or East Orebodies at Bayan Obo (Fig. 1). This paper presents a full textural, compositional and ²³²Th–²⁰⁸Pb age characterization of the occurrence in the context of the Proterozoic host rock suite and the REE mineralization and discusses REE behaviour throughout the geological history of the zircon. Trace element compositions in zircons from a variety of igneous rock types are listed by Belousova et al. (2002) and evaluated for their use as source indicators. Partitioning behaviour of trace elements between zircon and magmas associated with carbonatitic systems remains poorly understood, as no experimental data have been produced, and other

indicators, relating to REE partitioning between immiscible silicate–carbonatite melts, are limited (Blundy and Dalton 2000; Blundy and Wood 2003; Chakhmouradian and Williams 2004; Chakhmouradian 2006; Chakhmouradian and Zaitsev 2012; Rodionov et al. 2012; Veksler et al. 2012; Martin et al. 2013). However, Chakhmouradian (2006) states that partitioning of the high-field-strength elements (HFSE) that include the HREE are controlled by charge constraints relating to the crystallographic environment, and in general, carbonatitic HFSE are considered to originate from partial melting of metasomatized mantle sources (Chakhmouradian 2006; Blundy and Dalton 2000). Zr/Hf ratios exceeding 32 are reported for carbonatitic zircon based on a small number of occurrences. Particularly scarce are discussions of zircon-associated xenotime (e.g. Spandler et al. 2004; Wall et al. 2008), but new and deeper understanding of the behaviour of the HREE is evident in Williams-Jones et al. (2012) and the deposit-specific references therein.

The understanding of zircon alteration has advanced rapidly in recent times, not least because of deeper experimental and theoretical insights into element speciation and mobility in hydrothermal systems (Williams-Jones et al. 2012) but also because of major advances in analytical capabilities. A collection of papers on the mineralogy and geochemistry of zircon has been produced by Hanchar and Hoskin (2003), with a further, shorter, special issue introduced by Harley and Kelly (2007). Detailed compilations

and reviews of zircon textures (Corfu et al. 2003), and the presentation of recrystallization mechanisms (Geisler et al. 2007), are especially pertinent to the present study of the Bayan Obo zircon occurrence. Textural analysis of zircon has sustained major advances in recent years, in part, due to an increasing recognition of the possibility of hydrothermal/fluid alteration processes affecting this resilient mineral. Use of CL imagery and spectral analysis has also contributed to a new understanding of growth, recrystallization and alteration histories of zircons from many geological settings. While a high confidence in radiometric dating studies of zircons undoubtedly remains, textural analyses along with trace element data serve to support and fine-tune their findings.

Geochronological studies from Bayan Obo are best summarized in Fig. 4 of Kynicky et al. (2012), in Smith et al. (2014), and a brief overview is given in Table 1 (this paper). Whole rock ages tend to cluster in the 1,200–1,400 Ma range, but some older dates are reported from nearby rocks. It is clear that there is a better consensus on the age of the main mineralizations (broadly Caledonian, ~400–550 Ma) than on the age and origin of the host rock protolith. This is addressed in the present study with SHRIMP II ^{232}Th – ^{208}Pb analyses of two generations of East Orebody (unit H8) zircon. Advances in zircon isotopic systems (Scherer et al. 2007; Condon and Schmitz 2013), robust characterizations of standards (e.g. Compston 2001) and data processing methods (Sambridge and Compston 1994; Sircombe 2004) are considered in relation to the ^{232}Th – ^{208}Pb geochronological data of this study.

Methods

Fieldwork in the Main, East and West Orebodies and nearby carbonatite dyke outcrops was conducted for the collection of rock samples from in situ exposures and loose boulders, and GPS (global positioning system) data were collected. The location of each site was further determined by descriptive field notes (those of the present author and of Paul Henderson), supported by unpublished Chinese maps, mining company information and images from Google Earth as shown in Fig. 1.

The backscattered electron (BSE) images were undertaken on analytical scanning electron microscopes, operating at 15 keV. Colour cathodoluminescence (CL) images were collected using a Nuclide Corporation Luminoscope operating at 11.5 keV and 8 mA, and attached to a petrological microscope. Daylight print and slide photographic films were used (mostly 400ASA) as well as digital photography. Typical film exposure times ranged from 20 to 120 s. Colour CL imagery allows for visualization of sector zoning and of textural variation in hue, supported by

quantification of differences with the collection of CL spectra. The CL spectral investigation was undertaken courtesy of Oxford Instruments, using their Jeol 840A SEM operating at 15 keV, 0.3 nA and fitted with a MonoCL2 detector. Slits were set at 100 and 250 μm according to sensitivities for each grain. The spectral scans on single spots were taken across a wavelength range of 250–700 nm. The monochromatic greyscale images depict CL signals at two different wavelengths: 578.7 and 405 nm. These spectral data provide information aiding interpretation of changes in the distribution of REE activators of CL in the zircon structure, and they also aid consideration of defect-related luminescence (Nasdala et al. 2003), which can lead to grain-edge artefacts.

EPMA spot analyses and element maps were undertaken using a Cameca SX50 electron microprobe operating at 20 keV and 15 nA. In Online Resource 1, analytical parameters are given (standards, crystal detectors, X-ray lines and relevant interferences, investigated empirically and corrections applied). Inclusions in zircon and other accompanying mineral phases were semi-quantitatively characterized by energy dispersive spectrometry (EDS) on a Hitachi S2500 SEM at 20 keV.

Trace elements, including the full range of REE, were obtained by laser ablation-inductively coupled plasma-mass spectrometry (LA-ICP-MS) on 30 and 10 μm spots using a ESI (New Wave Research) UP193FX excimer laser coupled to an Agilent 7500cs ICP-MS housed in the Natural History Museum, London. This has a pulse width of <4 ns and a homogenized beam. The transport gas used in the cell was He at a flow rate of 0.44 l min^{-1} , mixed prior to the torch with Ar at a flow rate of 1.1 l min^{-1} . Stable ablation was achieved at a laser fluence of 3.3 J cm^{-2} and frequency of 10 Hz. Element ratios to an internal standard isotope (^{29}Si) were determined by referencing background-corrected integrated intensities from zircon signals to the external calibration standard NIST612 glass. Absolute element concentrations were then calculated from Si concentrations determined by EPMA in the programme ExLAM (Zachariáš and Wilkinson 2007). Limits of detection were set at the conventional 3σ of the background signal variation (Longerich et al. 1996). The NIST612 glass was also used to assess instrument precision and to monitor any effects of spot size (none were evident). Zircon 91500 (Wiedenbeck et al. 2004) was used as a secondary standard. Analyses of the standards are given in Online Resource 2, and the REE are shown with the working values for zircon 91500 from Wiedenbeck et al. (2004). Error bars shown for standard 91500 working values represent the combined effects of sample heterogeneity and interlaboratory variations (Wiedenbeck et al. 2004). Determinations made for the present study are well within these uncertainties, but it was noted that for the mid-heavy REEs (Eu–Lu), results for

the 10 micron spots appear slightly lower than those for the 30 micron spots. This apparently systematic error is significantly less than the errors associated with heterogeneity of standard 91500 or the range in detected values from natural samples.

A number of non-formula elements (e.g. Na, Ca, Fe, Ba) were determined to help monitor possible contamination of the sample analyses by inclusions, and these have been included in the tables. Abrupt changes in the signals during ablation also provided evidence that grain boundaries to inclusions had been encountered. Time-resolved raw cps signals were rigorously scrutinized and analyses with significant contamination were discarded outright. Contaminants expected were baryte, REE-ore minerals (fluorocarbonates and monazite), apatite, alkali silicates and magnetite. In the case of xenotime, veins and larger inclusions are readily identified from X-ray mapping, but YPO_4 is also likely to be in solid solution with ZrSiO_4 here (see later discussion on Er^{3+} activation of CL in a zircon matrix). Although the maximum available number of time slices (m/z sweeps) was always selected for integration, in most cases only short sections (≈ 10 – 40 time slices rather than ideally >40) of “clean” (contaminant-free) zircon signal could be resolved from the ablation traces from this small texturally complex grain. While counting statistics—a major contribution to uncertainty for elements close to the LOD—will be degraded and a certain degree of scatter introduced to the dataset, tests on the continuous “clean” signal from 91500 zircon have shown that detected concentration values stabilize between 4 and 12 integrated time slices for the various REE elements. For the Bayan Obo sample, analytical scatter was most significant for the LREE, and in particular, for La close to the LOD, limiting the use of these data in discrimination diagrams based on LREE ratios (Hoskin 2005). For the middle and HREE, and despite the time-slice issues described above, systematic variations between core and rim values indicated that the data could be grouped into discrete populations outside the range of analytical scatter, and these populations are presented in the “Results” section.

Radiometric dating was undertaken by sensitive, high-resolution ion microprobe (SHRIMP II) analysis (Compston et al. 1984; Ireland and Williams 2003) using the ^{232}Th – ^{208}Pb system due to insufficient U (<1 ppm) for the more conventional dual dating method using ^{238}U – ^{206}Pb and ^{235}U – ^{207}Pb . The beam current was 3–8 nA, and an initial spot size of 20 μm was used, later increased to 30 μm for improved sensitivity. The Th content of zircon was variable, and usable analyses were limited by detectability (>7 ppm). Online Resource 3 lists data from 39 SHRIMP spots on the QGNG zircon standard, analysed alternately with every two analyses of the sample. This was for close referencing and adjustments in relation to instrument drift

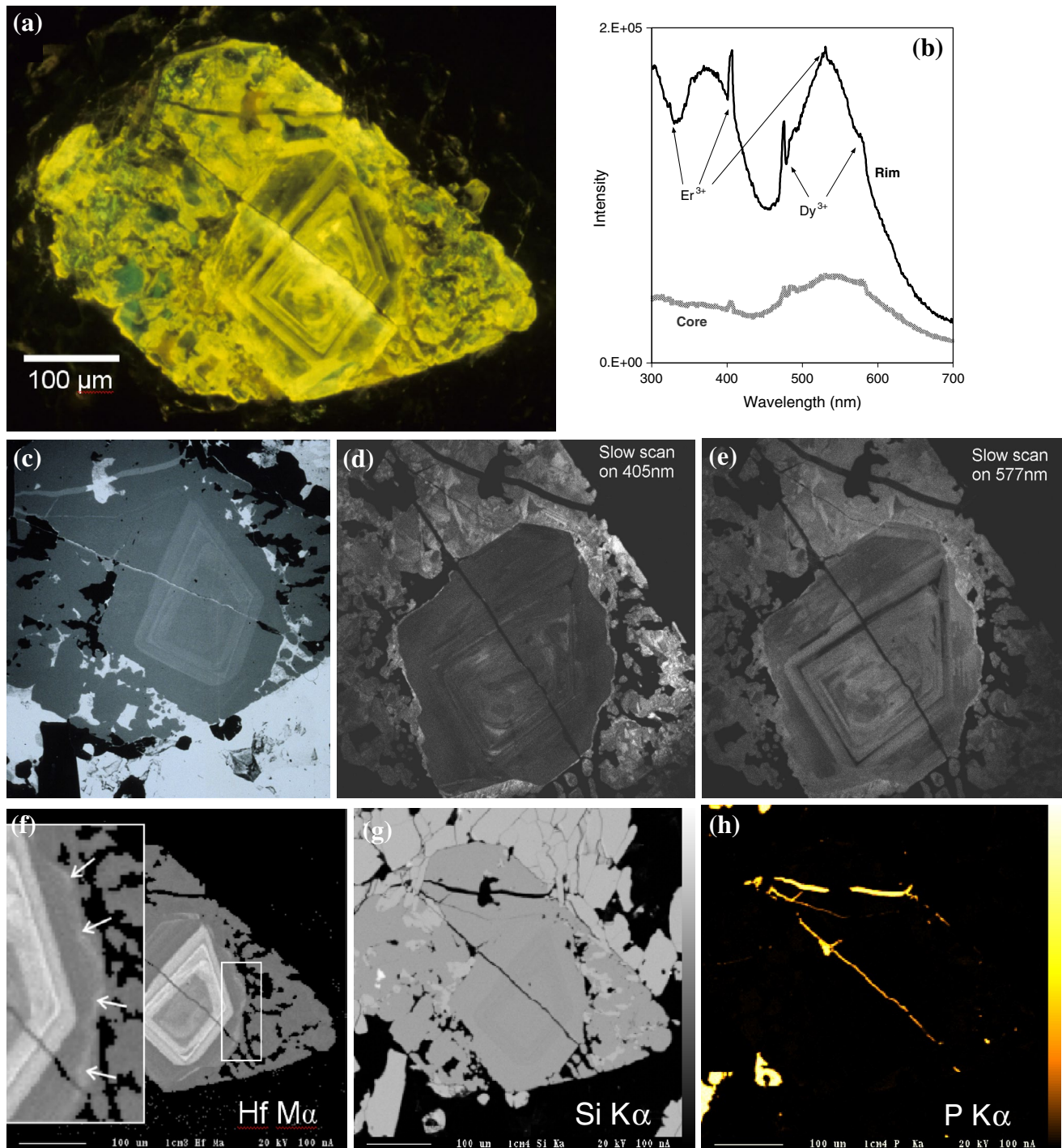
monitoring and for precision in evaluation of the age of the QGNG standard (Compston 2001). The QGNG isochron plots for three sessions are presented with the tables in Online Resource 3. Details of the analytical methodology and data processing procedures (mixture modelling, probability density distributions) are given in Compston et al. (1984), Sambridge and Compston (1994), Compston (2001) and Sircombe (2004).

Samples and field context

The Main and East Orebodies at Bayan Obo display prominent, fine-scale compositional banding (magnetite, apatite and fluorite), generally planar but with notable undulating and boudinage-like features, and cut by later generations of fluorite and aegirine–apatite veins (reviewed in Smith et al. 2014). These “banded ores” are also rich in REE fluorocarbonates and monazite. Zircon is highly restricted in occurrence to one main rock specimen, BM 1996, P4 (24) (in the collection of The Natural History Museum, London), from the 1,582 m level, East Orebody, north side (Fig. 1b), and to a second, very minor occurrence nearby, in BM 1995, P3 (39). The mineral assemblage in the main sample is dominated by apatite, REE fluorocarbonates and aegirine, giving it a green–brown appearance. Magnetite and fluorite are also present but less abundant than in other rocks typical of the banded ores. Monazite is widespread, fine-grained, disseminated and often occurring as inclusions in apatite. Sample BM 1995, P3 (39) contains sparse 10–30- μm zircon fragments that tend to occur as clusters enclosed by massive fluorite. The assemblage is dominated by fluorite, carbonates (calcite, dolomite and REE-enriched), apatite and alkali silicates. A lineated fabric is apparent, in line with fluorite-dominant bands up to a few millimetres thick. No zircon was found in any of the other rock specimens that were collected from close by [BM 1996, P4 (11), BM 1996, P4 (12) and BM 1996, P4 (25)] or elsewhere from within the NHM Bayan Obo collections.

Textural characteristics and zircon paragenesis

Bayan Obo zircon displays multiple textural characteristics, recording a long and varied geochemical history. Two main generations are described, representing preserved magmatic and post-magmatic events. Zircon grains range in size from 200 to 700 μm , and elongation ratios average 1.42, with a range of 1.1–1.7 (see Corfu et al. 2003). Key recurrent textural features described below are illustrated in Fig. 2 and also in Online Resource 4 where locations of SHRIMP analysis spots are shown. Undulating growth zonation in the very centres of cores is seen in BSE contrast and by



CL intensity contrast. These zones do not appear to have any relationship to crystal-face development and represent the earliest formed parts of the grains, interpreted as due to igneous resorption processes. Mineral inclusions found in cores include aegirine, aegirine–augite, and a hint of phlogopite from minor K and Al peaks in the EDS spectrum. In contrast to the inner cores, oscillatory zonation in the outer cores is highly euhedral, followed by an abrupt change to

a relatively thick band of apparently unzoned zircon. This specific pattern of growth periodicity is repeated in many grains. Core sector zoning, where present, is displayed almost exclusively by CL intensity contrast. Truncation features are seen within the zoned cores and particularly at interfaces with a distinct separate growth of rim zircon, mantling the cores. In some places, the transition from core to rim growth appears continuous (Online Resource 4 by

◀ **Fig. 2** Textural features of Bayan Obo zircon and accompanying mineral phases from rock BM 1996, P4(24). **a** Panchromatic cathodoluminescence (CL) image. **b** SEM-CL spectral profiles taken from two spots on an equivalent grain, core and rim, and applicable to images **a**, **d** and **e**. A distinct change is illustrated in CL emission spectra from core to rim in the *blue* range (~320–420 nm) showing high intensities of blue in rim zircon only. Broad-band *yellow* CL (~450–650 nm) is variably seen in both core and rim zircon. Superimposed on the broad-band emissions in the spectra, are finely resolved peaks at 405–407 and 475 nm, with an additional peak in the rim at 531 nm. The 405 nm peak is attributed to Er^{3+} activation (see “Discussion” in text). **c** Backscattered electron (BSE) image. Bright phases are REE-ore minerals, plus minor baryte. Baryte is paragenetically late, partially replacing a REE-mineral inclusion and vein–xenotime in the “£”-shaped feature, top left. Some very rounded patches of rim zircon are seen well in BSE, for example, in the far right and the lower left of image **c**. **d**, **e** SEM-CL: wavelength-specific images at 405 nm (*blue*) and 577 nm (*yellow*). Note that the HREE-enriched xenotime veins are non-luminescent. **f** Hf $M\alpha$ X-ray map showing euhedral, oscillatory growth zonation. Enlarged inset shows inward-penetrating Hf enrichment zones aligned with the irregular core–rim boundary. *Arrows* depict the likely direction of progression of a reaction front. **g** Si $K\alpha$ X-ray map showing abundant aegirine external to, and as inclusions in, rim zircon. Some aegirine crystals overprint rim zircon and the xenotime vein (*upper left* of image). **h** P $K\alpha$ X-ray map depicting xenotime veins and, *lower left*, apatite grains. Xenotime here is paragenetically bracketed by rim zircon (earlier), and aegirine and baryte (later)

scale bars). Mostly, however, the interface is irregular, giving more rounded outlines to the cores, and marked by a high intensity of CL emissions in the yellow band. Very intense CL emissions are also seen along planar fractures and around mineral inclusions, and this is consistent with increased crystal defect concentrations in these locations (Corfu et al. 2003). Inward-penetrating core–edge features as shown especially well in the Hf X-ray map (Fig. 2f) testify to a narrow reaction zone of about 10–20 μm in which Hf atoms have apparently been redistributed parallel to the core–edge interface. Implications of this are discussed later in the interpretation of processes.

The thickness of rim zircon is highly variable, and sometimes volumetrically significant relative to their cores. Although the rim features around many of the grains mimic the “cauliflower” zircons seen in Corfu et al. (2003) and Geisler et al. (2007), the “polycrystalline/multifaceted” types reviewed by these authors are different from those seen in the present study. This is because of the observed optical continuity with core zircon and because of the partial outer face development, generally of single, large crystals. However, rim growth is irregular, patchy and accompanied by abundant intergrowths and inclusions, including aegirine, bastnäsite, parisite, xenotime and baryte. Xenotime is also present as cross-cutting veins through core and rim zircon (Fig. 2c BSE and 2 h P $K\alpha$ X-ray map). A macroporosity can be seen in rim growth (e.g. Online Resource 4), texturally very similar to that seen in Putnis (2002). Rims are not zoned, but the CL patterns are mottled

and random. Rim fragments frequently occur as rounded masses, as seen in the far right of BSE image Fig. 2c. Parts of the rim zircons display bluer hues in CL, consistent with comparative CL spectral data (Fig. 2a, b, d). In the ~500 μm vicinity of many grains is the occurrence of ~10–20 μm angular fragments of zircon. These fragments are best observed using CL imagery, as they stand out in high CL contrast to all other mineral phases in these rocks, including luminescent apatite and fluorite. They appear to be texturally similar to sparse zircon fragments occurring in sample BM 1995, P3 (39).

Zircon compositions

Electron microprobe analyses of zircon are shown in Table 2, grouped into core and rim data and a traverse set of 16 analyses running from core to rim (see Online Resource 5 for spot locations and a compositional profile for the major elements). Atoms per formula unit calculated to four oxygens indicate consistently a slight depletion of Si + P in the tetrahedral sites. This imbalance could be due to some of the REE or non-formula elements existing in interstitial sites, or as microinclusions of other phases (e.g. ThO_2). Cores typically contain 2–7 wt% HfO_2 , varying with oscillatory growth zonation. Rim Hf averages 2.2 wt% HfO_2 , less variable than in the cores, consistent with textures observed by BSE imagery. The Hf $M\alpha$ X-ray map (Fig. 2f) demonstrates oscillatory fluctuation of Hf with the growing zircon crystal. It also provides compelling evidence for redistribution of Hf at the core–rim interface, in a reaction zone of ~10 μm thickness. Yttrium was rarely detected by EPMA in core zircon, but appeared as 0.1–0.2 wt% Y_2O_3 in the rims, mostly accompanied by P_2O_5 indicating zircon–xenotime-coupled substitution $\text{ZrSiO}_4 \leftrightarrow \text{YPO}_4$ in solid solution. Alternatively, an increased presence of xenotime microinclusions in a purer ZrSiO_4 lattice (Geisler et al. 2007) would give the same data. Neither Th nor U was detected by EPMA.

Trace element data determined from LA-ICP-MS analyses are given in Table 3 grouped into core and rim data, and equivalent summary data from carbonatitic (Yuan et al. 2008; Rodionov et al. 2012) and alkali pegmatitic zircons (Soman et al. 2010) are also listed. Figure 3a demonstrates the positive correlations between Y, Sc and ΣREE in zircon cores, indicating adherence to geochemical behaviour as a group. The correlation remains strong for Y and ΣREE in rim zircon but not for Sc (Fig. 3b), and this is most likely to be related to the very high charge/radius ratio for Sc, enhancing its hydrothermal complexation stabilities over the other trivalent REE and allowing it to remain in solution in conditions where the other REE are precipitated (Williams-Jones et al. 2012). A discrimination diagram defined

Table 2 Electron microprobe analyses including a core to rim traverse of zircon

Oxide weight %	Core to rim traverse in 64.5 microns													Cores				Rims								
	9	10	11	12	13	14	15	16	17	18	19	20	21	22	23	24	1	2	3	4	8	25	26			
SiO ₂	0.067	32.03	31.92	31.47	31.96	32.08	31.93	31.72	31.81	32.24	32.35	31.86	32.12	31.94	31.74	32.28	32.1	31.9	31.5	32.58	32.25	32.03	31.49	31.97		
ZrO ₂		64.24	62.31	61.68	61.93	63.55	61.69	62.42	65.38	65.78	66.05	65.82	65.05	65.35	65.33	65.67	65.36	61.81	62.45	66.3	64.14	65.79	66.15			
HfO ₂		0.324	3.889	7.018	7.192	8.18	4.798	6.505	6.384	2.48	2.247	2.432	2.177	1.772	1.537	1.812	1.972	6.803	6.906	2.102	2.485	4.818	1.703	1.415		
FeO ^b		0.11														0.114								0.866	0.436	
Y ₂ O ₃		0.039							0.047												0.08				0.123	0.214
La ₂ O ₃		0.078																								
P ₂ O ₅		0.050	0.051	0.063	0.052		0.089	0.07	0.072												0.131				0.065	0.146
Totals		100.2	101.3	100.4	102.1	100.5	100.2	100.6	99.71	100.3	100.8	99.86	100.3	99.67	99.1	100.1	99.81	100.7	100.9	100.4	101	101	100	100	100.3	
Molecular formula based on 4 oxygens																										
Zr		0.97	0.943	0.944	0.935	0.958	0.939	0.949	0.988	0.986	0.986	0.991	0.977	0.983	0.987	0.983	0.982	0.937	0.95	0.977	0.987	0.965	0.993	0.99		
Hf		0.034	0.062	0.064	0.072	0.042	0.058	0.057	0.022	0.02	0.021	0.019	0.026	0.016	0.014	0.016	0.017	0.06	0.061	0.018	0.022	0.042	0.015	0.012		
Y									0.001				0.001	0.006	0.004	0.004	0.002	0.002		0.001				0.002	0.003	
La																										
Σ A-site		1.004	1.005	1.008	1.007	1	0.997	1.006	1.011	1.006	1.007	1.01	1.004	1.005	1.005	1.003	1.001	0.999	1.011	0.996	1.009	1.007	1.01	1.005		
Si		0.992	0.99	0.988	0.99	0.992	0.997	0.989	0.986	0.991	0.991	0.984	0.99	0.986	0.984	0.991	0.989	0.992	0.982	0.997	0.985	0.988	0.975	0.981		
P		0.001	0.002	0.001		0.002	0.002	0.002					0.002	0.006	0.006	0.003	0.004	0.003		0.003		0.002	0.004			
Σ T-site		0.993	0.992	0.989	0.99	0.994	0.999	0.991	0.986	0.991	0.991	0.984	0.992	0.992	0.99	0.994	0.993	0.995	0.982	1	0.985	0.988	0.977	0.985		
Zr/Hf		29	15	15	13	23	16	17	45	49	47	52	38	61	71	61	58	16	16	54	45	23	66	83		

Locations of analyses are shown in Online Resource 5

^a LOD = Mean blank + 3SD

^b Measured as Fe²⁺. See Droop (1987) for Fe³⁺ conversion. Only trace levels determined and attributed to magnetite contamination. Omitted from formula calculations

Other elements analysed but always beneath detection were: Nb₂O₅ <0.26, Ta₂O₅ <0.206, TiO₂ <0.076, ThO₂ <0.228, UO₂ <0.05, MgO <0.05, CaO <0.137, MnO <0.155 and PbO <0.251 (wt%)

Table 3 Trace elements in Bayan Obo zircon by LA-ICP-MS

No. of slices ^a	Cores														Mean rim C10, C11, C15	±2σ rim	Yuan et al. (2008)	Rodionov et al. (2012)	Soman et al. (2010) Zomba-Malosa
	outer core							Rims											
	C12b central	B07	C13	C14	Mean outer core	±2σ outer core	C07	C08	C10	C11	C15	Mud Tank	Kovdor	Zircon I					
10	40	12	25	0.169	0.051	8	9	14	29	14	0.320	0.543	0.02	0.16	0.7	27			
La	0.086	0.140	0.182	0.186	0.169	0.445	0.121	0.128	0.512	0.320	0.320	0.543	0.02	0.16	0.7	27			
Ce	1.41	0.520	0.732	0.615	0.622	3.56	0.649	3.15	0.983	3.68	2.60	2.86	1.43	6	647	219			
Pr	2.83	0.060	0.181	0.112	0.118	0.144	0.144	0.047	0.075	0.061	0.061	0.039	0.07	1	1.6	16			
Nd	1.51	1.13	1.33	1.07	1.18	0.784	0.784	0.459	1.80	0.925	1.67	1.52	1.06	6	17.1	84			
Sm	0.703	1.87	0.953	1.49	1.44	1.46	1.46	0.426	2.10	1.69	1.69	2.19	1.65	6	27	54			
Eu	3.02	1.38	0.992	0.833	1.07	0.453	0.331	1.87	0.595	2.60	1.69	2.03	1.14	4	3.6	10.0			
Gd	0.417	9.76	4.47	5.97	6.73	2.47	2.47	23.3	6.07	25.4	18.3	21.2	6.02	25	208	156			
Tb	6.94	3.03	1.39	1.85	2.09	2.28	0.701	15.3	3.90	14.6	11.3	12.8	1.76	7	62	41			
Dy	2.37	34.6	16.0	19.2	23.3	44.7	14.1	315	80.5	292	229	259	16.5	71	928	590			
Ho	7.34	9.78	4.62	5.73	6.71	21.2	6.01	143	38.4	128	103	113	4.82	22	354	232			
Er	1.50	36.2	15.3	24.5	25.3	118	34.0	691	226	635	518	507	16.8	89	1,850	1,357			
Tm	13.1	6.70	3.26	4.25	4.74	28.7	7.66	151	56.4	125	111	97.9	2.99	16	458	372			
Yb	2.81	54.4	25.5	31.4	37.1	272	75.0	1,148	481	989	873	696	24.9	110	3,607	3,051			
Lu	44.0	7.67	3.35	5.33	5.45	34.3	12.3	146	81.0	135	121	70.0	3.86	17	451	405			
ΣREE	167	78.2	103	116	116	531	151	2,641	976	2,356	1,991	83.03	379.8	8,615	6,614				
Sm/La _N	28.1	21.1	8.3	12.8	5.22	5.22	979	5.30	6.52	106.6	59.6	61.3	3.2						
Lu/La _N	316	525	177	276	742	742	979	6,105	2,548	1,507	6,203	144							
Lu/Gd _N	7.47	6.32	6.03	7.18	112	112	186	107	43	5.16	5.47	17							
Yb/Sm _N	8.63	29.1	26.7	21.1	186	186	461	1,129	471										
Y/Ho _N	0.89	0.82	0.81	0.89	0.90	0.90	0.90	0.83	1.04										

Table 3 continued

	Cores				Mean outer core	±2σ outer core	Rims	Rims					Mean rim ±2σ rim C10,C11,C15	Yuan et al. (2008)	Rodionov et al. (2012)	Soman et al. (2010)
	C12b	B07	C13	C14				C07	C08	C10	C11	C15				
No. of slices ^a	10	40	12	25			8	9	14	29	14					
Na		14.9			14.9											
Al		1.10	2.89		1.99	2.53										
Si ^b		148,900	148,300	149,600	149,167	1,501	148,300	148,300	148,300	148,300	148,300	148,300				
Ca																
Sc		84.5	233	153	174	186	106	109	150	97.3	128	125	53.0		23	158
Ti				4.74	4.74			3.92							521	529
Sr		0.665	0.200	0.367	0.191	0.253	0.198	0.682	0.277	0.185	0.326	0.256	0.141		3.0	11.0
Y		61.6	234	110	149	165	127	556	4,300	933	3,890	3,040	3,670		3.1	6.4
Nb		1.1	1.9	25.1	1.1	9.4	27.3	11.1	180	8.10	122	103	175		25,434	15,591
Sn		2.20	6.63	2.41	3.74	5.00	3.48		2.64	2.22		2.43	0.598		1,652	1,971
Ba		4.72	2.10	2.15	1.91	2.05	5.51				1.02	1.02				
Hf		47,600	18,300	18,900	17,300	18,100	1,640	14,400	13,700	11,700	13,800	13,100	2,330			
Pb		1.74	0.830	1.07	0.584	0.828	0.484	0.700	1.15		1.27	1.21	0.172		1.9	12.3
Th		5.32	5.74	5.71	4.26	5.24	1.70	14.6	33.2	2.55	37.1	24.3	37.9		14,237	15,116
U		0.010	0.125		0.067	0.163			0.438	0.049	0.323	0.270	0.400			
Th/U		478	45.7						75.8	51.7	115					

Concentrations in ppm, normalized to Si from EPMA data. Chondrite-normalized REE values for Fig. 3 are not listed but were calculated using the Boynton (1984) chondrite values

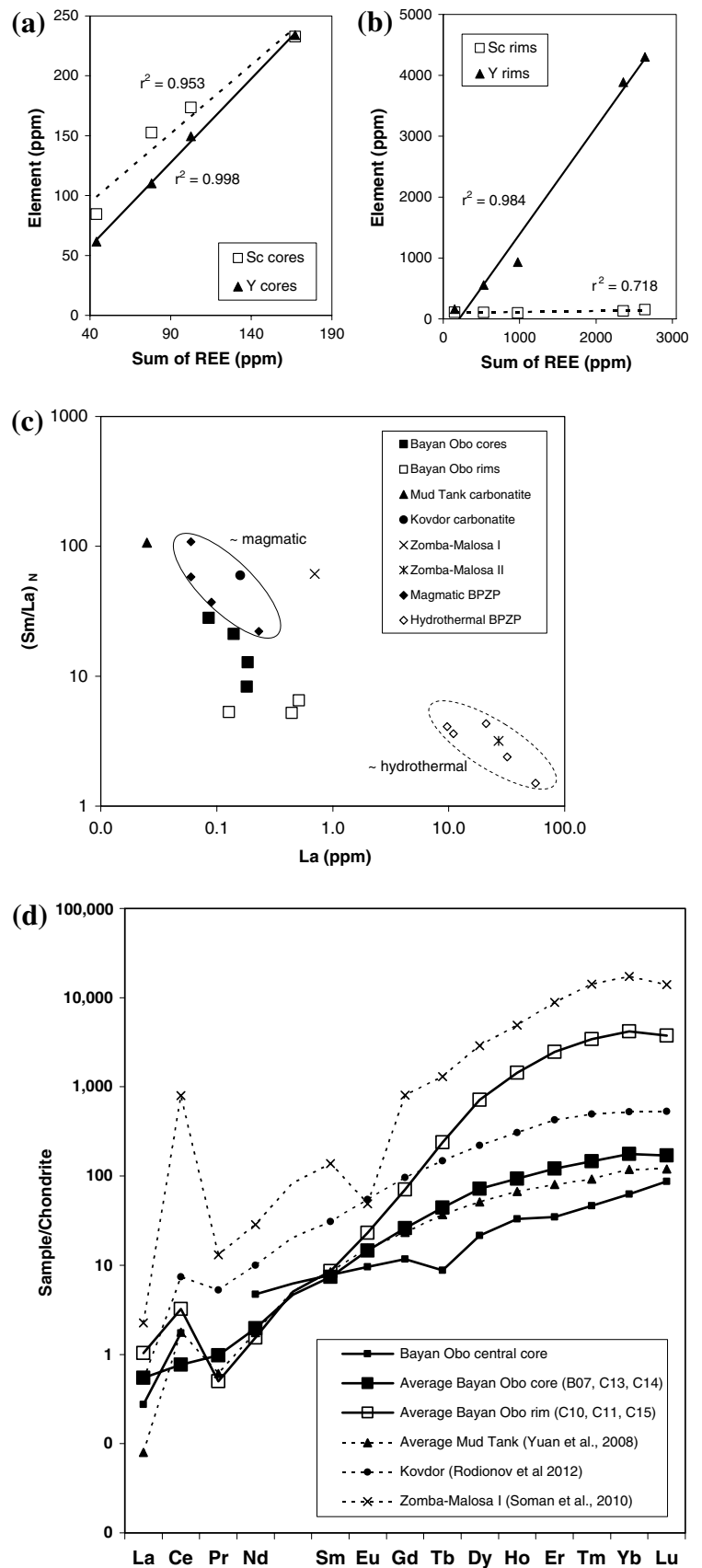
^a “No. of slices” refers to the integration interval, representing depth of ablation with time. Improved counting statistics are achieved with >20 slices, but >40 is optimal

^b Si taken from electron microprobe data

Fe, Mn and Ta were always below their detection limits (Fe: 8–91 ppm, Mn: 0.24–2.69 ppm and Ta: 0.012–0.137 ppm)

Subscript N = chondrite-normalized value

Fig. 3 Patterns of trace element data. **a** Y and Sc correlated with Σ REE, core zircon, **b** Y and Sc correlated with Σ REE, rim zircon. Increased hydrothermal stability of Sc over Y and Σ REE is indicated in its lower values and decreased correlation coefficient in rim zircon. **c** Tentative discrimination diagram (after Hoskin 2005) based on chondrite-normalized LREE ratios (Boynnton 1984 normalization data). Note discussion in the text on analytical uncertainty for the Bayan Obo LREE and La data, and discussion on coprecipitation of LREE phases with rim growth, both factors limiting the applicability of this type of discrimination for these particular zircons. **d** Chondrite-normalized REE diagram for Bayan Obo zircon (this study), for average Mud Tank Carbonatite zircon (Yuan et al. 2008), for Kovdor Carbonatite zircon (Rodionov et al. 2012) and for Zomba–Malosa alkaline pegmatitic zircon (Soman et al. 2010)



by Hoskin (2005) and based on LREE ratios tentatively places both core and rim data from Bayan Obo zircons close to the magmatic field (Fig. 3c). However, it was noted in separate tests that analytical scatter for the LREE, and especially for La being very close to the limit of detection, could be significant for the Bayan Obo data in which <40 time slices were possible to use. Therefore, the value of this type of discrimination for these particular data is limited. Very low values of La are nevertheless indicated and would tend to preclude any trend towards the hydrothermal field of Hoskin (2005). The overwhelming and independent evidence for major fluid events associated with the paragenetic stage in which rim zircon grew therefore requires deeper explanation. Firstly, the enhancement of HREE in the rims (Table 3; Fig. 3d) is consistent with the work of Smith et al. (2000) and Williams-Jones et al. (2012) in which high concentrations of mobilized REE, by F^- , CO_3^{2-} and phosphate complexation in hydrothermal/metasomatic fluids, precipitated as fluorocarbonate ore minerals (LREE, also monazite), and as solid solutions within zircon (HREE). Secondly, the intensity of LREE mineralization (bastnäsite, parisite, monazite, plus apatite to a lesser extent), displaying intimate intergrowths with rim zircon, would very likely provide an effective mineralogical buffer, specifically limiting LREE entry into zircon. Thus, the hydrothermal field of the Hoskin (2005) discrimination diagram based on $(Sm/La)_N$ versus La (ppm) may not be entirely applicable for zircons in strongly LREE-mineralized environments, as at Bayan Obo.

Figure 3d is a chondrite-normalized plot of the REE in Bayan Obo zircon compared with that of the Mud Tank carbonatite (Yuan et al. 2008), the Kovdor carbonatite (Rodionov et al. 2012) and the Zomba-Malosa alkali pegmatite (Soman et al. 2010). There is remarkable agreement between the average cores of Bayan Obo zircon with the average Mud Tank zircon, particularly with respect to Gd/Lu_N ratios and to the absence of Eu anomalies. A similar pattern is seen in the Kovdor carbonatitic zircon, but at increased levels of REE. Soman et al. (2010) data for zircon from an alkali pegmatite exhibit negative Eu anomalies and greater overall REE enrichment with higher Gd/Lu_N ratio (Table 3). The HREE are markedly raised in Bayan Obo rims by over one order of magnitude relative to the cores, with Lu/Gd_N ratios variable at 43–112 (rims) and consistent at 6–7 (cores). Chondrite-normalized LREE are similar in both cores and rims, except that a small positive Ce anomaly is apparent in rim zircon. Chondrite-normalized Y values are similar to those of Ho as often reported, due to ion size and charge similarity (Wall et al. 2008). It is important to note here that current understanding of partitioning behaviours of REE in zircon–carbonatite systems are limited, but a few studies have shown that they are not equivalent to those in zircon–silicate systems (Blundy and

Dalton 2000; Veksler et al. 2012, Martin et al. 2013). A full interpretation of the low LREE signatures in the magmatic core zircon therefore remains open.

Niobium, Ti and other HFSE are generally below 10 ppm, with the exception of two rim spikes for Nb; a moderate correlation between Th and Nb indicates possible aeschynite inclusions, or thorite where Th alone is raised. Aeschynite is known from the Bayan Obo deposit (e.g. Chao et al. 1997; Yang et al. 2001; Zhang et al. 2003; Smith and Spratt 2012) and reported as paragenetically related to the Caledonian events, consistent with zircon data of the present study. Cesbron et al. (1993) remark on the possibility of $(Ta, Nb)^{5+}$ balancing REE^{3+} in the zircon crystal structure, and this is also a possibility at the trace levels of Nb under consideration as well as various discussions on non-stoichiometry and interstitial sites (Hoskin and Schaltegger 2003). Insufficient data for Ti, either in this study or for other zircons in carbonatitic systems, precludes any attempt at its use as a geothermometer at present. Uranium concentrations were consistently under 1 ppm in both cores and rims, similar to extreme depletions in the Mud Tank and Kovdor zircons (Yuan et al. 2008; Rodionov et al. 2012), and raising important implications for magma and fluid sources over protracted timescales (see “Discussion”).

^{232}Th – ^{208}Pb SHRIMP II geochronology

It is assumed from the textural study that radiometric ages of only two geological events are recorded in the zircons of Bayan Obo, and these are (1) the igneous crystallization of the core, and (2) the alkaline alteration of the later epitaxial rim growth. ^{232}Th – ^{208}Pb isotope ratios for the Bayan Obo zircon samples are presented in Table 4, grouped by 19 core analyses and 12 rim analyses. Isochrons presented in Fig. 4(a) cores, and (b) rims, represent two distinct age populations. Initial Pb ($^{208}Pb/^{204}Pb$) data are given in Online Resource 6. With a limited data set comprising a range of “age components”, a mixture modelling approach was applied to the evaluation and presentation of the geochronological data (Sambridge and Compston 1994), in addition to simpler averages and weighted means, and the results are compared in Table 5. From the probability density distributions in Fig. 5, the core crystallization date is $1,324.7 \pm 4.12$ Ma based on one assumed age. The quoted ± 4 Ma precision on this 1,325 Ma age is numerically correct based on statistical analysis of the ^{232}Th – ^{208}Pb data, and on rationalization of a single age component (see below), but it is misleading, giving an inappropriate impression of very high precision. We consider that this is most likely due to the probable “chance” symmetry in the data distribution (Fig. 5a histogram part), where two peaks straddle the 1,325 Ma result. Taking account of

Table 4 Summary SHRIMP data grouped by core and rim spots

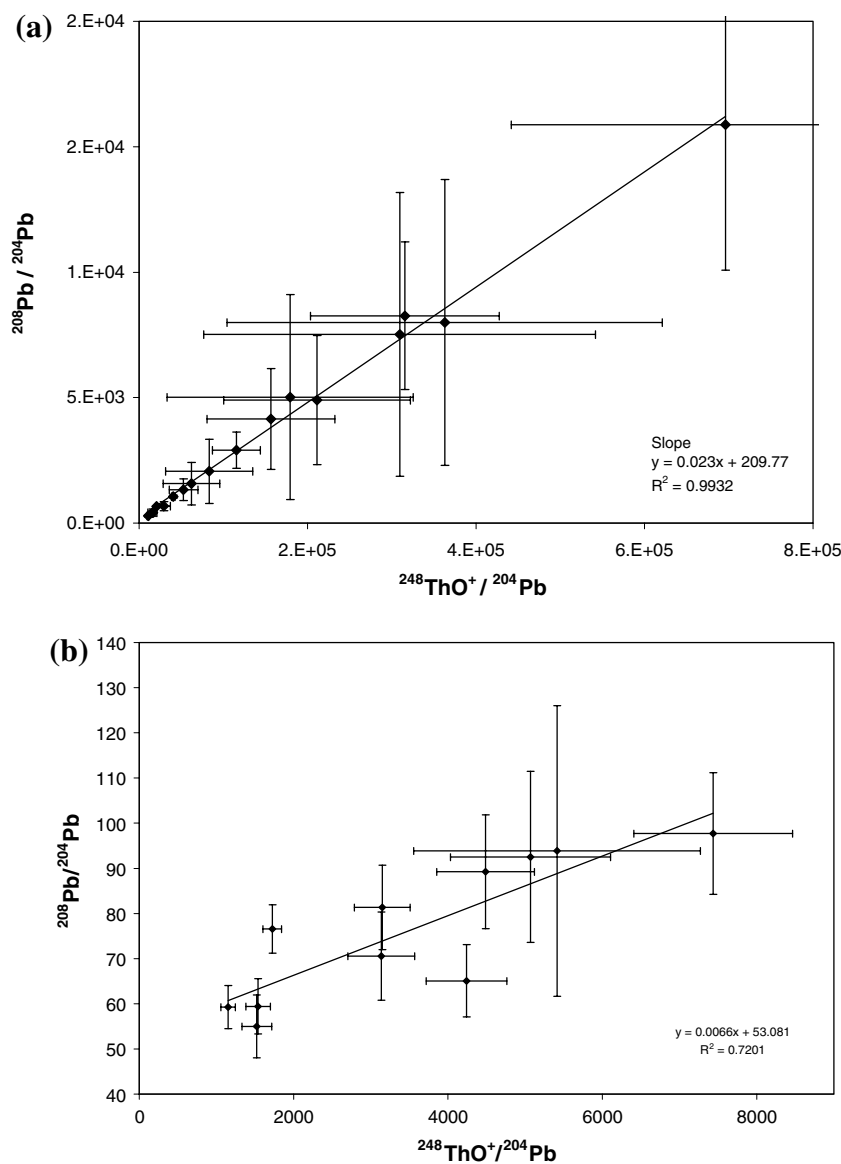
Spot	248/204	±	208/204	±	Th ppm	Age	±
<i>Cores</i>							
C-2	20,835	871	663.57	27.74	650.0	1,493.5	6.4835
C-3	7.68E+06	2.56E+06	166,670	55,556	261.5	1,140.5	5.6128
C-5	40,597	2,264.9	1,052.6	58.726	867.2	1,375.8	5.6904
C-7	29,205	7,875.6	672.49	181.35	15.2	1,397.1	42.455
C-15	3.42E+06	3.90E+08	1.00E+05	1.14E+07	8.4	1,481.7	82.115
D40	1.56E+05	75,873	4,149.4	2,014.4	162.5	1,336.7	12.34
D41	15,852	5,422.8	423.37	144.83	16.8	1,354	55.271
D42	62,146	33,561	1,569.9	847.77	56.1	1,280.6	22.877
J-16	1.16E+05	28,543	2,907	718.29	261.5	1,363.4	7.3574
J-17	10,734	1,445.6	282.33	38.021	47.6	1,295	30.382
J-18	1.79E+05	1.46E+05	5,025.1	4,090.8	107.7	1,476.6	12.145
J-19	83,119	51,585	2,061.9	1,279.6	88.0	1,381	19.96
J-20	52,757	17,143	1,326.3	430.95	92.3	1,344.4	15.538
J-21	2.11E+05	1.11E+05	4,902	2,571.1	221.5	1,289.8	7.7497
J-22	16,534	1,967.7	420.52	50.045	129.2	1,254.4	17.565
N-24	6.96E+05	2.54E+05	15,873	5,794.9	1,108	1,263.5	4.1464
N-26	3.15E+05	1.12E+05	8,264.5	2,937	553.9	1,436.2	4.8779
O-23	3.09E+05	2.33E+05	7,518.8	5,653.2	156.9	1,276.1	17.769
P-25	3.63E+05	2.58E+05	8,000	5,696	341.5	1,212.1	7.6916
Rims							
C-12	4,240.8	522.75	65.083	8.0226	19.0	286.53	60.71
C-13	1,523.3	193.27	54.996	6.9778	5.4	501.93	187.46
C-14	3,135.8	433.9	70.562	9.7637	9.5	499.96	96.851
C-29	1,150.3	93.055	59.266	4.7946	8.0	776.45	141
C-30	1,724.2	121.04	76.558	5.3746	20.4	936.64	77.113
C-31	3,148.3	362.02	81.321	9.3509	31.8	639.48	94.697
C-32	5,414.4	1,855.8	93.853	32.168	5.8	617.42	164.51
C-33	1,540	158.96	59.421	6.1331	9.6	654.72	150.3
D-37	7,063.9	2,206.4	155.09	48.441	8.9	886.19	101
D-38	7,435.8	1,027.4	97.714	13.501	24.4	422.73	42.906
D-39	4,488.2	633.21	89.238	12.59	17.7	546.85	83.097
E-35	5,068	1,037.5	92.507	18.938	8.9	545.57	89.899

²³²Th measured as ThO⁺ for the 248/204 listing. Standard error denoted as “±”. Data exclude 4 core and 7 rim spots that had poor counting statistics, mainly due to Th < 7 ppm. Other outliers were included in the data set, but large errors were noted for C3, C15 and J18

this, the limitations of the Th–Pb system, and of the very small data set available, we therefore suggest a less precise 1325 ± 60 Ma, as the best present estimate of the timing of the core zircon crystallization. One assumed age for the core data is texturally justified, despite the double-peak histogram distribution in Fig. 5a. A further justification for assuming one core age is given in Fig. 5b, where approximate core spot locations are shown in relation to results <1,325 Ma or >1,325 Ma (individual spot ages are listed in Table 4). It can be seen that no pattern is apparent. With reference to Table 4, note that two outliers (C3 at 1,140.5 Ma and C15 at 1,481.7 Ma) both have large errors on the ^{208/204}Pb ratio. Analysis C15 additionally is based on a very low Th concentration (8 ppm). Figure 5c is a cumulative probability density distribution for the rim

spots. The rim age of 455.6 ± 28.27 Ma is considered to be the best estimate of true age, based on an assumption of two distinct age components (Table 5) where the second age component of 876 Ma is acknowledged as resulting from 3 suspect analyses that probably intersected inclusions or pores, had disturbed Pb, or perhaps contained older, xenocryst fragments; (see spots C29, C30 and D37 in Online Resource 4). Nevertheless, the presence of older fragments would be partially aligned with a reported Neoproterozoic metamorphic event of 809 ± 80 Ma (Zhang et al. 2003), based on Sm–Nd and placed in overall geochronological context by Smith et al. (2014). An alternative interpretation using the same data (this zircon study), but based on an assumption of one distinct age is 537.3 ± 24.08 Ma).

Fig. 4 ^{232}Th – ^{208}Pb isochrons for Bayan Obo zircon: **a** cores, **b** rims. ^{232}Th measured as $^{248}\text{ThO}^+$



Discussion

The highly localized distribution of zircon at Bayan Obo, together with core-growth textures and compositions, is consistent with an overall interpretation of a suite of small-intrusive alkaline–carbonatitic rocks, and its accompanying wide envelope (spatially and temporally) of fluid-dominant mineralization and fenitization. The lack of clear, field-observed intrusive rock boundaries in the East Orebody at Bayan Obo is by no means conclusive evidence that such boundaries did not exist. Fenitization and other fluid-rich reactive processes with intense deformation are likely to have obliterated sharp boundaries otherwise observable at field scale. At the grain scale, the possibility of zircon metamictization by alpha particle emitters is generally ruled out for the Bayan Obo zircons because their compositions are strongly depleted in U

and also very low in Th. This has implications for the interpretation of zircon paragenesis, and for the evaluation of CL emissions, as metamictization can contribute to quenching of the CL signal in zircon (Nasdala et al. 2003). In the following discussion, nuances of CL emissions are evaluated, core–rim interface issues are explored, and a geological history is outlined, followed by special attention to the source magma and the mineralization.

Interpretation of cathodoluminescence imagery and spectra

Zircon has been the subject of a considerable body of cathodoluminescence (CL) studies due to its excellent and varied luminescent properties and its relative durability enabling their preservation. Many textural, spectral and experimental (doping) studies have been undertaken

Table 5 Comparative evaluations of SHRIMP data

Type of evaluation	Data origin	No. of data points	No. of assumed ages	Age (Ma)	±	p	±	Negative log likelihood	Degrees of freedom	Chi square
Mean	Cores	19	1	1,339.6	94					
Weighted mean		19	1	1,366.2	1.94					
PDD		19	1	1,324.7	4.12	1	0.22	1,520.03	18	168.89
PDD		1	4	1,140.5	5.61	0.053				
		4	4	1,458.65	3.71	0.202	0.11			
		7	4	1,366.31	3.99	0.372	0.148			
		7	4	1,260.03	3.46	0.374	0.155	82.7	12	13.783
Mean	Rims	12	1	609.54	43.81					
PDD		12	1	537.3	24.08	1		34.02	11	6.185
PDD		3	2	876.47	67.36	0.279				
		9	2	455.64	28.27	0.721	0.259	15.17	9	3.371

Statistical parameters and results for one and four assumed ages for cores, and for one and two assumed ages for rims. Our best present estimate of the core age is $1,325 \pm 60$ Ma, with a lower recommended precision than calculated, accounting for the limitations of this small data set in the distribution of data (see explanation in the text). The second assumed age component in the rims is represented by three outlying rim analyses which are attributed either to older fragments or, more likely, to Th contamination from inclusions such as monazite or aeschynite. Ages in bold are considered to be the best estimates of true core-growth and rim-alteration ages

PDD probability density distribution

in recent years, described and evaluated in Nasdala et al. (2003). In addition, MacRae and Wilson (2008) provide a useful database applicable to CL and other luminescence techniques for a wide variety of minerals and materials, with a review by Götze (2012) on CL applications in the geosciences. Of relevance to the present work are references to broad-band yellow and blue CL and narrow-band emissions centred on 405, 475 and 530 nm.

In the core zircon, CL emissions are generally seen to be in the yellow region, and this is confirmed by the broad-band spectrum peaking between 500 and 600 nm (Fig. 2b). Although some yellow CL in zircon is attributed to “intrinsic emissions”, as seen in pure, undoped, synthetic ZrSiO_4 (Rémond et al. 1995), the textures displayed indicate additional causes. Most strikingly, the core–rim boundaries exhibit very intense yellow CL, rapidly decreasing in intensity away from the edges (the core side of the interface). So high is the intensity that bright reflections are seen in the surrounding grain boundaries (e.g. Fig. 2a). This is reasonable to expect, given that escape depths of CL signals are considered to be relatively large (Nasdala et al. 2003). According to Götze et al. (1999), such broad-band yellow CL is attributed to defects on the tetrahedral SiO_4 groups. Rémond et al. (1995) in a CL study of REE-doped zircons also discuss the impacts of structural defects and other edge phenomena. High-defect concentrations at the core–rim interfaces of Bayan Obo grains are consistent, along with growth zone truncations, with degradation of cores. Defect-related CL is also consistent with the increased intensity of CL along some fractures (Fig. 2a). A third type of texture

in the Bayan Obo specimens giving broad-band yellow CL is thought to be chemical alteration effects, as described by Corfu et al. (2003) and experimentally by Geisler et al. (2003). The expression of alteration is seen as inward-penetrating bulbous fronts and feathery features that superimpose fine-scale core zonations and that also engulf the blue/blue–green CL of the patchy rim growth to give a mottled appearance. Narrow-band yellow CL is evident from the growth textures and CL spectra, most notably in the fine-scale oscillatory, and sector zoning (Fig. 2 and Online Resource 5). These bright zones are attributed to activation by Dy^{3+} , with narrow-band peak clusters centred on 480 and 580 nm (Cesbron et al. 1993; Hanchar and Marshall 1995; Götze et al. 1999; Richter et al. 2006; MacRae and Wilson 2008).

The broad-band blue CL (~300–450 nm) is most evident in the rim growth, and this type of emission is generally considered as “intrinsic”, as determined from studies on synthetic, pure zircons (Cesbron et al. 1993 and Götze et al. 1999). Additionally, Hanchar et al. (2001) found a dull, blue CL in synthetic zircons doped with “non CL active” La^{3+} and Yb^{3+} . In Nasdala et al. (2003), broad-band blue CL is demonstrated in spectra of two Australian zircons, from the McBride Province, and from the Mud Tank carbonatite. In neither of these examples is a very intense blue band seen, and Nasdala et al. (2003) attribute this partly to the relatively more intense yellow band emissions in most zircons and partly to the general decrease in instrument sensitivities at wavelengths in the blue region. Despite this, the relatively high-intensity broad-band blue emission of

the Bayan Obo rim zircon (Fig. 2b) stands in marked contrast to previous reports and warrants further consideration of causes related to trace element composition. The strong, narrow-band peak at 405 nm and a weaker one at 325 nm (Fig. 2b), together with the trace element findings of this study (Table 3; Fig. 3), testify to increased HREE involvement in rim growth, since in a study on REE-doped zircons, Cesbron et al. (1993) demonstrated major peaks for Er^{3+} at these wavelengths, supported by Richter et al. (2006) and MacRae and Wilson (2008). A third major Er^{3+} peak is listed at 480 nm by Cesbron et al. (1993), but is considered unresolvable with the Dy^{3+} narrow-band cluster and generally intense broad-band yellow CL in this wavelength region. Nasdala et al. (2003) list another Er^{3+} peak at 530 nm (after Rémond et al. 2000), which could account for the pointed shape at the apex of the broad-band yellow emission seen in Fig. 2b.

Further, unique value of the monochromatic CL images is in the evaluation of phases present. It has been discussed as to whether the $(\text{Y, HREE})\text{PO}_4$ component of microprobe and LA-ICP-MS data for the rim zircon is present in true solid solution with ZrSiO_4 or as microinclusions of xenotime enclosed within purer zircon, according to the dissolution–reprecipitation reaction mechanism of Geisler et al. (2007). The evidence from Fig. 2d (image of the 405 nm emission in which xenotime appears dark, but bright in the P $K\alpha$ map, Fig. 2h) and from Fig. 2b (broad-band blue emission that distinguishes zircon from xenotime, Richter et al. 2006) is that the CL activator, Er^{3+} , is operating absolutely within the mineralogical context of zircon in true solid solution and not occurring as a separate phase of xenotime. This finding does not undermine significant other lines of evidence for reaction of zircon at Bayan Obo; it merely indicates that the zircon rims had equilibrated with fluids rich in P and REE, distinct from the older magmatic growth, and that preserved reaction zones from later dissolution processes were narrow (~ 10 – $20 \mu\text{m}$ as described earlier).

Deductions from the core–rim interface

The dramatic change in characteristics between core and rim zircon is worthy of special attention. Firstly, it needs to be stated that the coexisting preservation of euhedral crystal faces of core growth alongside oscillatory zone truncations and irregular edges, together with the absence of radial fractures and an appropriate mineral assemblage, all precludes any notion of sedimentary abrasion. Instead, a corroding fluid attacking both cores and rims and actively precipitating new phases could conceivably achieve both the irregular and crystal-face sensitive morphologies observed. These resultant paradoxical textures are best explained with reference to heterogeneous properties of

the compositionally variable core zircon lattice. A corrosion interpretation is supported by recent developments in the understanding of zircon alteration and fluid-rich dissolution–reprecipitation reaction fronts (Geisler et al. 2007), which appear to explain the interface-parallel (inward-penetrating) zones, where Hf has apparently been locally redistributed (Fig. 2f). The examples demonstrate the close relationship of the reaction front to the dissolved edge behind it and support the hypothesis of zircon reaction with a fluid. The fragmentary nature (including rounding) of rim zircon together with the CL evidence of inwardly penetrating bulbous fronts (Corfu et al. 2003) also support an interpretation of reaction and dissolution, and demonstrate that the expression and extent of corrosion vary with subtleties of zircon composition and properties, with rims having been preferentially altered over cores.

Geological history

(i) Early magmatic growth ($1,325 \pm 60 \text{ Ma}$)

In the central parts of zircon cores, the undulatory resorption textures seen are indicative of a magmatic environment, where episodic periods of Zr undersaturation in the magma are likely to have occurred (Corfu et al. 2003). Immediately beyond these central zones, the ubiquitous oscillatory compositional zonation seen would have been governed by processes at the crystal–melt interface (e.g. diffusion rates, Zr and Hf saturation and redox conditions, Corfu et al. 2003; Harley and Kelly 2007). Hoskin (2000) further suggested that “external” (magma system) processes such as differentiation can control the ordering of oscillatory zonations in zircon. This is largely supported by Fowler et al. (2002), in their interpretation of “thick harmonic zones” as evidence of large-scale periodic change in the magma system. In contrast, their high-resolution, fine-scale oscillatory zonations were attributed to crystal–melt interface dynamics (Hoskin 2005). In the present study, the observed periodicity in core-growth patterns most notably highlights a limited stage during which fine-scale oscillatory growth occurred, where compositionally oscillating growth was sensitive to the immediate environment at the crystal/melt interface, particularly with respect to Zr/Hf ratios and probably also of REE as evidenced by CL. The incorporation of REE into the zircon structure as a solid solution in the well-documented xenotime substitution, $\text{REE}^{3+} + \text{P}^{5+} = \text{Zr}^{4+} + \text{Si}^{4+}$, is dependent on an adequate supply of P to the crystal/liquid interface, and this is partly controlled by the diffusion rate of P relative to crystal growth (Hoskin 2000). However, Cherniak and Watson (2003) note that charge balancing for the REE does not necessarily need to come from P in a coupled substitution; it may occur with O-site defects or hydroxyl groups.

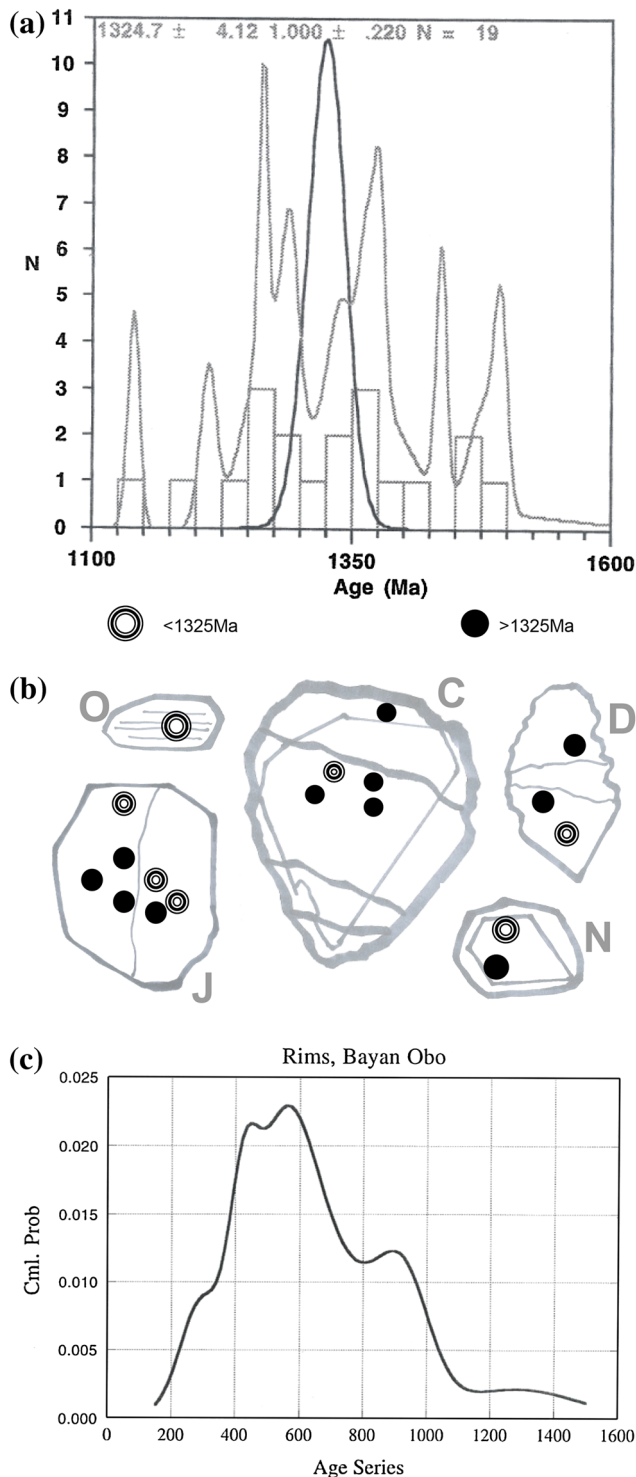


Fig. 5 **a** Probability density distribution (PDD) of SHRIMP Th–Pb data overlaying age component histogram for 19 core components, assuming one true age. The multi-peaked curve represents the cumulative probability. See Compston et al. (1984) and Sircombe (2004) for a full discussion of the procedure and its advantages over simple histogram presentations. **b** SHRIMP spot positions in relation to age results of individual data points. Just one assumed age is justified from the textural information, in which no spatial pattern is evident from the pre- and post-1,325 Ma age results. **c** Cumulative probability curve for 12 rim ages, resolved into two age components at 456 and 876 Ma (explanation in the text and in Table 5)

carbonatitic zircons (Yuan et al. 2008, Rodionov et al. 2012) and tentatively fit in the magmatic field of the Hoskin (2005) discrimination diagram based on LREE ratios. Niobium concentrations in Bayan Obo zircon cores are much lower than in the alkaline rock zircons of Soman et al. (2010), and Ta was not detected at all. Belousova et al. (1998) discuss Nb/Ta in zircon, highlighting the probable influence of Nb minerals in carbonatitic environments, on the ratio.

The low elongation ratios of Bayan Obo core zircons, coupled with the major and trace element compositions, are indicative of intrusive, possibly plutonic, magmatic growth (Corfu et al. 2003), and this has implications for our understanding of the origin of the protolith suite of the Bayan Obo Fe–Nb–REE deposit. The pyramid-dominant morphology is also significant because of its possible association with melts of kimberlitic–alkaline–carbonatitic origin.

(ii) Epitaxial overgrowths (rims)

The characteristics of rim zircon growth in terms of compositions, morphology, intergrowths, CL colours, zoning patterns and radiometric age collectively support a metasomatic secondary growth and fluid alteration explanation, contemporaneous with the main REE–fluorocarbonate mineralization event reported by (Chao et al. 1992; Wang et al. 1994; Campbell and Henderson 1997 and Kynicky et al. 2012), and are indicative of a fluid with significant activity of P. Evident from the preservation of volumetrically significant “new” bipyramidal crystal forms outlining rim zircon, it is deduced that there must have been a period in which thick, sub- to euhedral overgrowths, abundantly intergrown with REE (ore) and other minerals, developed around the magmatic cores. The apparent smooth growth transition from core to rim seen in a few places suggests that zircon precipitation (rather than degradation) was dominant at this time, and the promotion of outer crystal-face development suggests growth in an open fluid environment, perhaps analogous to the residual fluids fractionated from a melt as in the model of Harley et al. (2007) in their Fig. 1, stage F. Although this model of Harley et al. (2007) is of a high-temperature terrain, the equivalent (carbothermal

The sector zoning seen in the Bayan Obo cores, and probably caused by REE variation as it is not apparent on the Hf X-ray maps, is similarly attributed to current hypotheses on diffusion kinetics and differential growth rates of crystal faces (Fowler et al. 2002; Corfu et al. 2003).

Chondrite-normalized REE patterns in Bayan Obo cores are well matched with the Mud Tank and Kovdor

fluids) in an alkaline–carbonatitic system at lower temperatures might be envisaged (Fan et al. 2006; Smith 2007; Williams-Jones et al. 2012). Such residual fluids are likely to have concentrated the REE, leaving their signature in the overgrowths. The expression of this at Bayan Obo is in the abundant REE-ore mineral intergrowths with rim zircon (LREE-enriched bastnäsite, etc.), and in the rim compositions where the sum of the lanthanide group elements plus P is higher than in the cores and where HREE are enriched ($(\text{Lu/Gd})_N$ 43–112). Apatite is also abundant, rich in REE and intergrown with rim zircon (see type II apatite of Campbell and Henderson 1997), highlighting the role of P in the system at this stage. It is considered likely that the age of the epitaxial overgrowths was reset during an aegirine alteration stage which partially dissolved zircon (see below).

(iii) Metasomatism (455.6 ± 28.27 Ma)

Evidence of remobilization of HREE is in secondary xenotime occurring as cross-cutting veins through zircon (also as inclusions) and first reported in Campbell (1998). It raises the question of reactive processes occurring subsequent to rim growth. According to the Geisler et al. (2007) model, non-metamict, trace element-rich (solid solution) zircon is replaced by trace element-poor, purer zircon, with the formation of secondary phases derived from the components of solid solution. In an environment dominated by the LREE, it is deduced that components for locally precipitated xenotime could have been derived from the P + Y + HREE-enriched rim zircon determined in this study as well as by mineral-controlled fractionation from the REE fluids. Direct evidence for zircon degradation of Bayan Obo cores has been seen in the Hf $M\alpha$ X-ray map of Fig. 2f, where Hf distribution is related to the irregular core–edge surface rather than the crystal growth zones seen nearby. The only way in which Hf atoms could move in this 10–20- μm reaction front is with the breakdown of the zircon structure, if only temporarily, in a dissolution–reprecipitation-type mechanism after Geisler et al. (2007). Unlike Hf, however, it is suggested that some Y + HREE was locally mobilized and reprecipitated as a separate phase of xenotime, explaining the veins observed. It is further suggested that rim zircon was much more susceptible to alteration and dissolution than core zircon for the following reasons: (1) its skeletal habit, intensively intergrown with other phases giving a high surface area to its grain boundaries; (2) its macroporosity; and (3) its composition relating to $\text{Si}^{4+} \leftrightarrow \text{P}^{5+}$ substitution, HREE enrichment and possible lattice stress/defects from small stoichiometric imbalances. Evidence from CL colours showing patches of blue rim growth edged by bulbous yellow alteration fronts resembling some of the experimental findings of Geisler

et al. (2003), supports this interpretation. Thus, aggressive fluids capable of dissolving silicates, selectively corroded rim zircon over core zircon (though both generations were attacked), releasing pre-concentrated HREE for localized reprecipitation as xenotime. Such processes, in which Zr and other HFSE can be remobilized in appropriate fluid-rich environments, are consistent with reports of hydrothermal remobilization processes concentrating the HREE in new mineral phases, as in Sheard et al. (2012), and with the experimental fractionation of REE in an alkali-P system (Williams-Jones et al. 2012). Paragenetically late aegirine overprinting zircon and xenotime, seen in the Si $K\alpha$ map (Fig. 2g), is suggestive of pervasive alkaline fenitization affecting the zircon-bearing rock. Moreover, the high activity of Na^+ in this fluid (Smith 2007) might have contributed to its dissolving power. This would be consistent with the association of melt peralkalinity and zircon saturation (Watson and Harrison 1983), but in a fluid context. It is also consistent with the age of aegirine veins reported by Chao et al. (1997) as 438 ± 25 Ma (late Caledonian); the Type III apatites of Campbell and Henderson (1997) in aegirine veins; and the post-banding stage 3 aegirine veins and alteration of Smith (2007) and Smith et al. (2014). Fluorite occurrence in this rock is also indicative of fluid compositions, paragenetically multipulsed, both earlier and later than the aegirine stage.

Source magma

In view of the growing body of evidence that the Bayan Obo region has seen multiple episodes of carbonatitic activity (e.g. Drew et al. 1990; Campbell and Henderson 1997; Yang et al. 2003; Mitchell 2005; Yang and Woolley 2006; Le Bas et al. 2007; Kynicky et al. 2012; Smith et al. 2014) and that the world-class REE-ore mineral deposits there mainly originate from carbonatite-derived fluids (e.g. Fan et al. 2006; Smith 2007), a comparison of zircons in the present study with those of known carbonatitic association (Mud Tank and Kovdor) is essential. A further imperative to this evaluation is that questions still remain about the determination of the host rock protolith suite and deformation at Bayan Obo.

In a detailed review of the mineralogy of high-field-strength elements in carbonatitic and phoscoritic rocks, Chakhmouradian and Williams (2004) stated that the chemical evolution of zircon in carbonatite melts is not well known. They describe many reports, however, of zircon of undoubted primary magmatic origin (e.g. Claesson et al. 2000), especially where there is an accompanying assemblage that includes silicates such as phlogopite. Some characteristics of zircons from known kimberlite–alkaline–carbonatite systems documented in the literature (Belousova et al. 1998; Claesson et al. 2000; Belousova et al. 2002;

Corfu et al. 2003; Chakhmouradian and Williams 2004) are that they tend to form large (>250 μm), bipyramidal, stubby forms. The work of Page et al. (2007) on kimberlitic zircons from four continents supports these observations and confirms further the common occurrence of oscillatory growth zoning with sharp truncations where only fragments of the megacrysts remain. The zircons of the present study compare well with some of these characteristics, especially with respect to the lack of prism face development and the low elongation ratios (“stubby” forms). While the ~ 700 μm lengths of the largest Bayan Obo zircons do not approach the megacrystic, cm-scale proportions of the kimberlitic zircons described by Belousova et al. (1998) and Page et al. (2007), they do tend to exceed the upper limit of ~ 200 μm for zircons in “common rocks” as reported by Corfu et al. (2003).

In terms of chemical compositions, low Hf contents are observed in zircons from kimberlite–alkaline–carbonatite systems (<2 wt% HfO_2 from Kola, Chakhmouradian and Williams 2004, and <1wt% from Lofdal, Namibia, Wall et al. 2008) and Zr/Hf ratios of 30–41 in Belousova et al. (1998). The Bayan Obo zircon with its high Hf content (up to 7wt% HfO_2 and Zr/Hf ratios averaging only 24 in the cores with a median of 16) is not consistent with this pattern, and instead, might indicate a fractionated melt where the Zr/Hf ratio has decreased relative to chondritic values of 37 (Hoskin and Schaltegger 2003). High Th/U ratios (or very low U) are reported in zircons from kimberlite–alkaline–carbonatite systems (Davis 1977; Belousova et al. 1998, 2002; Chakhmouradian and Williams 2004; Page et al. 2007). Specifically, Yuan et al. (2008) list U concentrations in zircon averaging 50 ppm for the Mud Tank carbonatite and 9 ppm for the Monastery kimberlite. For Kovdor, U is extremely depleted at <1 ppm (Rodionov et al. 2012). Together with the trace element data of the present study, this bears consistency with the wider context of reported Th/U ratios at Bayan Obo (Chao et al. 1992; Wang et al. 1994; Chao et al. 1997) and with a lithospheric mantle or lower crustal source. Rare earth partitioning in zircon–melt systems is discussed by Hanchar and van Westrenen (2007), generally supporting the known preference for HREE in the zircon structure. Although equivalent data for trace element partitioning between zircon and non-silicate melts remain unknown, Chakhmouradian and Zaitsev (2012) describe recent research on REE behaviours and immiscible melts. They explain that trace element patterns derived from element partitioning models, and experimental data from Veksler et al. (2012), are suggestive of strong partitioning of REE into the silicate phase in immiscible carbonate–silicate systems. These findings are consistent with experimental data of Martin et al. (2013), who further report that increased REE partitioning into a carbonatite melt can occur with higher SiO_2 contents of the immiscible

silicate melt. The presence of water also increases REE partition coefficients for a carbonatite melt in a carbonatite–silicate system (Martin et al. 2013). Conversely, in immiscible fluoride–silicate and phosphate–silicate systems, the REE partition preferentially into the non-silicate phase (Veksler et al. 2012). These recent discussions further indicate some evidence for LREE–HREE fractionation, HFSE fractionation and variable behaviours of alkali-group elements—all being sensitive to bulk melt compositions and to the hydrous status of the system. Such complexities in carbonatitic systems, which are only just beginning to be investigated, thus limit the present discussion on petrogenetic context of the rare Bayan Obo zircons. However, the absence of an Eu anomaly is indicative of a plagioclase-free melt, suggesting silica-undersaturation in the magma from which zircon crystallized, and matching well with the REE composition of zircon from the Mud Tank and Kovdor carbonatites (Yuan et al. 2008; Rodionov et al. 2012).

Relationship of zircon growth history to the rare earth mineralization

Key papers in the Bayan Obo literature refer to a “main mineralization event” for the formation of the highly enriched (up to several wt% RE_2O_3) bastnäsite–parisite–monazite dominant REE mineralization occurring in the Main and East Orebodies at Bayan Obo (e.g. Chao et al. 1992; Wang et al. 1994; Chao et al. 1997). However, it is established that significant REE mineralization (monazite occurrence) was in the late Mesoproterozoic, explained in the review by Smith et al. (2014). Nevertheless, Wang et al. (1994) date the main metasomatic, REE-ore concentrating event as Caledonian, around 555–420 Ma on the basis of ^{232}Th – ^{208}Pb analyses of monazite, and it is thought by some authors to be penecontemporaneous with major, possibly subduction-related tectonic shearing at this time (Chao et al. 1997). Temperatures in the range ~ 250 – 480 $^\circ\text{C}$ for the main mineralization have been constrained by various fluid inclusion and mineral reaction studies (e.g. Smith et al. 1999; Smith and Henderson 2000; Fan et al. 2006; Qin et al. 2007), and by thermodynamic modelling of silicate assemblages (Smith 2007). These temperatures further support a fluid-dominant, metasomatic origin for the rim zircon assemblage. The main ore-deposition stage also links paragenetically with the type II apatites of Campbell and Henderson (1997) because of their intergrowth occurrence and REE-enriched compositions. The findings of Smith et al. (2000), relating REE ratios in Bayan Obo mineral compositions to fluid evolution, are partially mirrored in the HREE enrichment of the present zircon rims. Smith et al. (2000) reported La–Nd ratios as ~ 3 – 7 in early monazite (attributed to CO_2 fluids) and ~ 0.6 – 2 in late REE fluorocarbonates (attributed

to more aqueous fluids). Zircon REE patterns with secondary xenotime occurrence are also consistent with new experimental data in Williams-Jones et al. (2012), which demonstrate temperature-sensitive REE fractionation with progressive fluid–rock interaction in a P–NaCl system, and the tendency for HREE to remain in the local “input zone”. So the rim zircon age (455.6 ± 28.27 Ma) of the present study is considered to be related to the aegirine overprint, in which the earlier epitaxial rim growth was reset. Corrosive fluid infiltration relating to reactive degradation of zircon, locally mobilizing Y and HREE and precipitating late xenotime veins and aegirine (requiring a high activity of Na^+ , Smith 2007), is also indicated in Wang et al. (1994) at 430–420 Ma, closely matching that of the present study.

Conclusions

The zircon occurrence in the northern part of the East Orebody at Bayan Obo has provided a unique record of the early geological history of the region as well as providing a powerful set of data complementing rifting–magmatism models of the supercontinent Columbia in the Mesoproterozoic, and the existing consensus as to the Caledonian timing of the main, transformative and REE–ore concentrating mineralization events, and their alkaline–carbonatitic sources. The combination of imaging methods (BSE, CL and X-ray mapping) along with the determination of CL spectra, major and trace element compositions and ^{232}Th – ^{208}Pb ages have together enabled a detailed growth and degradation history to be determined and have highlighted some features of the geochemical behaviour of the REE. Bayan Obo zircon cores have been shown to represent part of a magmatic, intrusive, carbonatitic protolith suite that crystallized at $1,325 \pm 60$ Ma. Epitaxial mantles with increased (Y, HREE) PO_4 substitution crystallized during the main REE mineralization event and incorporated LREE–ore minerals and other phases as inclusions and intergrowths. Subsequent dissolution–reprecipitation processes by aggressive, Na–P–F-bearing fluids at 455.6 ± 28.27 Ma left evidence in (a) the inward-penetrating reaction fronts where Hf was locally redistributed; (b) the patchy rim textures, (c) CL features, (d) localized secondary xenotime veins derived from fluid reaction with HREE-enriched zircon rims, (e) the overprinting textures of the alkali silicate phases. The textural and geochemical signatures observed are testimony to the complexity of fluid-related processes repeatedly reported for the Bayan Obo mineralization (Kynicky et al. 2012; Smith et al. 2014). Nevertheless, they are consistent with previous reports on the evolution of ore fluids and with current

developments in the understanding of fractionation of individual REE in hydrothermal systems.

The notable scarcity of zircon occurrences at Bayan Obo and their diverse petrologic characteristics have together refocused attention on the nature of the protolith in the area of the banded orebodies. Such studies are very limited due to the lack of preservation of protolith components, but determination of protolith variations and characteristics is a challenge that could best shed light on the full origin of this world-class mineral deposit.

Acknowledgments Fieldwork was kindly supported by The Baotou Iron and Steel (Group) Company Ltd, Zhang Peishan, Yang Zhuming and their colleagues in the Institute of Geological Sciences, Chinese Academy of Sciences, Beijing, and Paul Henderson (The Natural History Museum, London). Funding for Linda Campbell’s fieldwork, and her visiting research fellowship to ANU, Canberra (SHRIMP analysis), was provided by The Royal Society. The minor revisions were completed at the University of Manchester with the support of NERC grant NE/L002418/1. All other work was largely unfunded, and so special acknowledgement is given to the following for collaborative support: X-ray mapping and EPMA analysis at The Natural History Museum with C. Terry Williams and John Spratt, CL spectroscopy at Oxford Instruments with Chris McLean, electron microscopy and research facilities from Andy Rankin (University of Kingston), LA-ICP-MS facility from Teresa Jeffries (Natural History Museum), data analysis support with Kerry Gallagher (Imperial College, London), image processing with Mark Danson (University of Salford) and also with Gordon Langridge (G Graphics), and general research facilities in Earth Sciences with Richard Patrick and others from the University of Manchester. Frances Wall (CSM, University of Exeter) is thanked for facilitating the LA-ICP-MS collaboration and for various useful discussions during the development of this work. Martin Smith (University of Brighton, UK) and Jindrich Kynicky (Mendel University in Brno, Czech Republic) are gratefully acknowledged for sharing their Bayan Obo expertise in further discussions, and some very useful comments of two reviewers and the editor have been gratefully welcomed, leading to improvements in the manuscript.

Open Access This article is distributed under the terms of the Creative Commons Attribution License which permits any use, distribution, and reproduction in any medium, provided the original author(s) and the source are credited.

References

- Belousova EA, Griffin WL, Pearson NJ (1998) Trace element composition and cathodoluminescence properties of southern African kimberlitic zircons. *Mineral Mag* 62(3):355–366. doi:[10.1180/002646198547747](https://doi.org/10.1180/002646198547747)
- Belousova EA, Griffin WL, O’Reilly SY, Fisher NI (2002) Igneous zircon: trace element composition as an indicator of source rock type. *Contrib Mineral Petrol* 143(5):602–622. doi:[10.1007/s00410-002-0364-7](https://doi.org/10.1007/s00410-002-0364-7)
- Blundy J, Dalton J (2000) Experimental comparison of trace element partitioning between clinopyroxene and melt in carbonate and silicate systems, and implications for mantle metasomatism. *Contrib Mineral Petrol* 139(3):356–371. doi:[10.1007/s004100000139](https://doi.org/10.1007/s004100000139)
- Blundy J, Wood B (2003) Partitioning of trace elements between crystals and melts. *Earth Planet Sci Lett* 210:383–397. doi:[10.1016/S0012-821X\(03\)00129-8](https://doi.org/10.1016/S0012-821X(03)00129-8)

- Boynton WV (1984) Geochemistry of the rare earth elements: meteorite studies. In: Henderson P (ed) Rare earth element geochemistry. Elsevier, Amsterdam, pp 63–114
- Campbell LS (1998) Zircon-fluid interaction in the Bayan Obo REE–Nb–Fe ore deposit, Inner Mongolia, China. In: Aреhart GB, Hulston JR (eds) Water rock interaction (Proceedings of the ninth international symposium on water-rock interaction), Balkema, pp 521–523
- Campbell LS, Henderson P (1997) Apatite paragenesis in the Bayan Obo REE–Nb–Fe ore deposit, inner Mongolia, China. *Lithos* 42(1–2):89–103. doi:10.1016/s0024-4937(97)00038-8
- Cesbron F, Ohnenstetter D, Blanc P, Rouer O, Sіchere MC (1993) Incorporation of rare-earth elements in synthetic zircons—a cathodoluminescence study. *Comptes Rendus De L Academie Des Sciences Serie Ii* 316(9):1231–1238
- Chakhmouradian AR (2006) High-field-strength elements in carbonatitic rocks: geochemistry, crystal chemistry and significance for constraining the sources of carbonatites. *Chem Geol* 235(1–2):138–160. doi:10.1016/j.chemgeo.2006.06.008
- Chakhmouradian AR, Wall F (2012) Rare earth elements: minerals, mines, magnets (and more). *Elements* 8(5):333–340. doi:10.2113/gselements.8.5.333
- Chakhmouradian AR, Williams CT (2004) Mineralogy of high-field-strength elements (Ti, Nb, Zr, Ta, Hf) in phosphoritic and carbonatitic rocks of the Kola Peninsula, Russia. In: Wall F, Zaitsev A (eds) Phoscorites and carbonatites from mantle to mine: the key example of the Kola Alkaline Province, vol. The Mineralogical Society of Great Britain and Ireland, London, pp 293–340
- Chakhmouradian AR, Zaitsev AN (2012) Rare earth mineralization in igneous rocks: sources and processes. *Elements* 8(5):347–353. doi:10.2113/gselements.8.5.347
- Chao ECT, Back JM, Minkin JA, Ren YC (1992) Host-rock controlled epigenetic, hydrothermal metasomatic origin of the Bayan Obo REE–Fe–Nb ore deposit, Inner-Mongolia, PRC. *Appl Geochem* 7(5):443–458. doi:10.1016/0883-2927(92)90005-n
- Chao E, Back J, Minkin J, Tatsumoto M, Wang J, Conrad J, McKee E (1997) The sedimentary carbonate-hosted giant Bayan Obo REE–Fe–Nb ore deposit of Inner Mongolia, China: a cornerstone example for giant polymetallic ore deposits of hydrothermal origin. U.S. Geological Survey bulletin 2143. United States Government Printing Office, Washington, p 65
- Cherniak DJ, Watson EB (2003) Diffusion in zircon. *Zircon* 53:113–143. doi:10.2113/0530113
- Claesson S, Vetrin V, Bayanova T, Downes H (2000) U–Pb zircon ages from a Devonian carbonatite dyke, Kola peninsula, Russia: a record of geological evolution from the Archaean to the Palaeozoic. *Lithos* 51(1–2):95–108. doi:10.1016/s0024-4937(99)00076-6
- Compston W (2001) Effect of Pb loss on the ages of reference zircons QGNG and SL13, and of volcanic zircons from the Early Devonian Merriams and Turondale Formations, New South Wales. *Aust J Earth Sci* 48(6):797–803. doi:10.1046/j.1440-0952.2001.00898.x
- Compston W, Williams IS, Meyer C (1984) U–Pb geochronology of zircons from lunar breccia 73217 using a sensitive high mass-resolution ion microprobe. *J Geophys Res* 89:B525–B534 (Supplement)
- Condon DJ, Schmitz MD (2013) One hundred years of isotope geochronology, and counting. *Elements* 9(1):15–17. doi:10.2113/gselements.9.1.15
- Corfu F, Hanchar JM, Hoskin PWO, Kinny P (2003) Atlas of zircon textures. *Zircon* 53:469–500. doi:10.2113/0530469
- Davis GL (1977) The ages and uranium contents of zircons from kimberlites and associated rocks. *Carnegie Inst Wash Yearbook* 76:631–635
- Drew L, Meng Q (1990) Geologic map of the Bayan Obo area, Inner Mongolia, China. In: Miscellaneous Investigations Series, Map I-2057, United States Geological Survey
- Drew LJ, Meng Q, Weijun S (1990) The Bayan Obo iron rare-earth niobium deposits, Inner-Mongolia, China. *Lithos* 26(1–2):43–65. doi:10.1016/0024-4937(90)90040-8
- Droop GTR (1987) A general equation for estimating Fe³⁺ concentrations in ferromagnesian silicates and oxides from microprobe analyses, using stoichiometric criteria. *Mineral Mag* 51:431–435. doi:10.1180/minmag.1987.051.361.10
- Ernst RE, Wingate MTD, Buchan KL, Li ZX (2008) Global record of 1600–700 Ma Large Igneous Provinces (LIPs): implications for the reconstruction of the proposed Nuna (Columbia) and Rodinia supercontinents. *Precambrian Res* 160(1–2):159–178. doi:10.1016/j.precamres.2007.04.019
- Fan HR, Xie YH, Wang KY, Tao KJ (2004) REE daughter minerals trapped in fluid inclusions in the giant Bayan Obo REE–Nb–Fe deposit, Inner Mongolia, China. *Int Geol Rev* 46(7):638–645. doi:10.2747/0020-6814.46.7.638
- Fan HR, Hu FF, Yang KF, Wang KY (2006) Fluid unmixing/immiscibility as an ore-forming process in the giant REE–Nb–Fe deposit, Inner Mongolian, China: evidence from fluid inclusions. *J Geochem Explor* 89(1–3):104–107. doi:10.1016/j.gexplo.2005.11.039
- Fowler A, Prokoph A, Stern R, Dupuis C (2002) Organization of oscillatory zoning in zircon: analysis, scaling, geochemistry, and model of a zircon from Kipawa, Quebec, Canada. *Geochim Cosmochim Acta* 66(2):311–328. doi:10.1016/s0016-7037(01)00774-8
- Geisler T, Pidgeon RT, Kurtz R, van Bronswijk W, Schleicher H (2003) Experimental hydrothermal alteration of partially metamict zircon. *Am Mineral* 88(10):1496–1513
- Geisler T, Schaltegger U, Tomaschek F (2007) Re-equilibration of zircon in aqueous fluids and melts. *Elements* 3(1):43–50. doi:10.2113/gselements.3.1.43
- Götze J (2012) Application of cathodoluminescence microscopy and spectroscopy in geosciences. *Microsc Microanal* 18(6):1270–1284. doi:10.1017/s1431927612001122
- Götze J, Kempe U, Habermann D, Nasdala L, Neuser RD, Richter DK (1999) High-resolution cathodoluminescence combined with SHRIMP ion probe measurements of detrital zircons. *Mineral Mag* 63(2):179–187. doi:10.1180/002646199548411
- Hanchar J, Hoskin P (eds) (2003) Reviews in mineralogy and geochemistry, Zircon, vol. 53 The Mineralogical Society of America, Washington DC
- Hanchar JM, Marshall DJ (1995) Multi-laboratory results for the cathodoluminescence emission spectrum from a synthetic zircon standard. *Luminescence*. In: Proceedings of the 13th Pfefferkorn conference pp 269–276
- Hanchar JM, van Westrenen W (2007) Rare earth element behavior in zircon-melt systems. *Elements* 3(1):37–42. doi:10.2113/gselements.3.1.37
- Hanchar JM, Finch RJ, Hoskin PWO, Watson EB, Cherniak DJ, Mariano AN (2001) Rare earth elements in synthetic zircon: part 1. Synthesis, and rare earth element and phosphorus doping. *Am Mineral* 86(5–6):667–680
- Hao Z, Wang X, Li Z, Xiao G, Zhang T (2002) Petrological study of alkaline basic dyke and carbonatite dyke in Bayan Obo, Inner Mongolia. *Acta Petrol Mineral* 21(4):429–444
- Harley SL, Kelly NM (2007) Zircon—tiny but timely. *Elements* 3(1):13–18. doi:10.2113/gselements.3.1.13
- Harley SL, Kelly NM, Moller A (2007) Zircon behaviour and the thermal histories of mountain chains. *Elements* 3(1):25–30. doi:10.2113/gselements.3.1.25
- Hatch GP (2012) Dynamics in the global market for rare earths. *Elements* 8(5):341–346. doi:10.2113/gselements.8.5.341
- Hoskin PWO (2000) Patterns of chaos: fractal statistics and the oscillatory chemistry of zircon. *Geochim Cosmochim Acta* 64(11):1905–1923. doi:10.1016/s0016-7037(00)00330-6

- Hoskin PWO (2005) Trace-element composition of hydrothermal zircon and the alteration of Hadean zircon from the Jack Hills, Australia. *Geochim Cosmochim Acta* 69(3):637–648. doi:10.1016/j.gca.2004.07.006
- Hoskin PWO, Schaltegger U (2003) The composition of zircon and igneous and metamorphic petrogenesis. *Zircon* 53:27–62. doi:10.2113/0530027
- Ireland TR, Williams IS (2003) Considerations in zircon geochronology by SIMS. *Rev Mineral Geochem Zircon* 53:215–241. doi:10.2113/0530215
- Kynicky J, Smith MP, Xu C (2012) Diversity of rare earth deposits: the key example of China. *Elements* 8(5):361–367. doi:10.2113/gselements.8.5.361
- Le Bas MJ (2008) Fenites associated with carbonatites. *Can Mineral* 46:915–932. doi:10.3749/canmin.46.4.915
- Le Bas MJ, Keller J, Tao KJ, Wall F, Williams CT, Zhang PS (1992) Carbonatite dykes at Bayan Obo, Inner-Mongolia, China. *Mineral Petrol* 46(3):195–228
- Le Bas MJ, Xueming Y, Taylor RN, Spiro B, Milton JA, Peishan Z (2007) New evidence from a calcite-dolomite carbonatite dyke for the magmatic origin of the massive Bayan Obo ore-bearing dolomite marble, Inner Mongolia, China. *Mineral Petrol* 90(3–4):223–248. doi:10.1007/s00710-006-0177-x
- Liu YL, Williams IS, Chen JF, Wan YS, Sun WD (2008) The significance of paleoproterozoic zircon in carbonatite dikes associated with the Bayan Obo REE–Nb–Fe deposit. *Am J Sci* 308(3):379–397. doi:10.2475/03.2008.08
- Longerich HP, Jackson SE, Günther D (1996) Laser ablation inductively coupled plasma mass spectrometric transient signal data acquisition and analyte concentration calculation. *J Anal At Spectrom* 11:899–904
- MacRae CM, Wilson NC (2008) Luminescence database I—minerals and materials. *Microsc Microanal* 14(2):184–204. doi:10.1017/s143192760808029x
- Martin LHJ, Schmidt MW, Mattsson HB, Guenther D (2013) Element partitioning between immiscible carbonatite and silicate melts for dry and H₂O-bearing systems at 1–3GPa. *J Petrol* 54(11):2301–2338. doi:10.1093/petrology/egt048
- Mitchell RH (2005) Carbonatites and carbonatites and carbonatites. *Can Mineral* 43:2049–2068
- Nasdala L, Zhang M, Kempe U, Panczer G, Gaft M, Andrut M, Plotze M (2003) Spectroscopic methods applied to zircon. *Zircon* 53:427–467. doi:10.2113/0530427
- Ni P, Rankin AH, Ling HF, Jiang SY, Jiang YH (2004) Carbonatitic magmatic fluid kept in quartzite associated with carbonatite dyke in Bayan obo, China. *Geochim Cosmochim Acta* 68(11):A301
- Nie FJ, Jiang SH, Su XX, Wang XL (2002) Geological features and origin of gold deposits occurring in the Baotou-Bayan Obo district, south-central Inner Mongolia, People's Republic of China. *Ore Geol Rev* 20(3–4):139–169. doi:10.1016/s0169-1368(02)00069-0
- Page FZ, Fu B, Kita NT, Fournelle J, Spicuzza MJ, Schulze DJ, Viljoen F, Basei MAS, Valley JW (2007) Zircons from kimberlite: new insights from oxygen isotopes, trace elements, and Ti in zircon thermometry. *Geochim Cosmochim Acta* 71(15):3887–3903. doi:10.1016/j.gca.2007.04.031
- Putnis A (2002) Mineral replacement reactions: from macroscopic observations to microscopic mechanisms. *Mineral Mag* 66(5):689–708. doi:10.1180/0026461026650056
- Qin CJ, Qiu YZ, Zhou GF, Wang ZG, Zhang TR, Xiao GW (2007) Fluid inclusion study of carbonatite dykes/veins and ore-hosted dolostone at the Bayan Obo ore deposit. *Acta Petrol Sin* 23(1):161–168
- Rémond G, Blanc P, Cesbron F, Ohnenstetter D, Rouer O (1995) Cathodoluminescence of rare earth doped zircons. II. Relationship between the distribution of the doping elements and the contrasts of images. *Scanning Microsc Suppl* 9:57–76
- Rémond G, Phillips MR, Roques-Carnes C (2000) Importance of instrumental and experimental factors on the interpretation of cathodoluminescence data from wide band gap materials. In: Pagel M, Barbin V, Blanc P, Ohnenstetter D (eds) *Cathodoluminescence in Geosciences*, Springer, Berlin, pp 59–126
- Richter DK, Krampitz H, Gorgen P, Gotte T, Neuser RD (2006) Xenotime in the Lower Buntsandstein of Central Europe: evidence from cathodoluminescence investigation. *Sediment Geol* 183(3–4):261–268. doi:10.1016/j.sedgeo.2005.09.017
- Rodionov NV, Belyatsky BV, Antonov AV, Kapitonov IN, Sergeev SA (2012) Comparative in situ U–Th–Pb geochronology and trace element composition of baddeleyite and low-U zircon from carbonatites of the Palaeozoic Kovdor alkaline–ultramafic complex, Kola Peninsula, Russia. *Gondwana Res* 21(4):728–744. doi:10.1016/j.gr.2011.10.005
- Sambridge MS, Compston W (1994) Mixture modeling of multicomponent data sets with application to ion-probe zircon ages. *Earth Planet Sci Lett* 128(3–4):373–390. doi:10.1016/0012-821x(94)90157-0
- Scherer EE, Whitehouse MJ, Munker C (2007) Zircon as a monitor of crustal growth. *Elements* 3(1):19–24. doi:10.2113/gselements.3.1.19
- Sheard ER, Williams-Jones AE, Heiligmann M, Pederson C, Trueman DL (2012) Controls on the concentration of zirconium, niobium, and the rare Earth elements in the Thor Lake Rare Metal Deposit, Northwest Territories, Canada. *Econ Geol* 107(1):81–104
- Sircombe KN (2004) AGEDISPLAY: an EXCEL workbook to evaluate and display univariate geochronological data using binned frequency histograms and probability density distributions. *Comput Geosci* 30(1):21–31. doi:10.1016/j.cageo.2003.09.006
- Smith MP (2007) Metasomatic silicate chemistry at the Bayan Obo Fe–REE–Nb deposit, Inner Mongolia, China: contrasting chemistry and evolution of fenitising and mineralising fluids. *Lithos* 93(1–2):126–148. doi:10.1016/j.lithos.2006.06.013
- Smith MP, Henderson P (2000) Preliminary fluid inclusion constraints on fluid evolution in the Bayan Obo Fe–REE–Nb deposit, Inner Mongolia, China. *Econ Geol Bull Soc Econ Geol* 95(7):1371–1388. doi:10.2113/95.7.1371
- Smith M, Spratt J (2012) The chemistry of niobium mineralisation at Bayan Obo, Inner Mongolia, China: constraints on the hydrothermal precipitation and alteration of Nb-minerals. *Dizhi Xuebao* 86(5):700–722
- Smith MP, Henderson P, Zhang PS (1999) Reaction relationships in the Bayan Obo Fe–REE–Nb deposit Inner Mongolia, China: implications for the relative stability of rare-earth element phosphates and fluorocarbonates. *Contrib Mineral Petrol* 134(2–3):294–310. doi:10.1007/s004100050485
- Smith MP, Henderson P, Campbell LS (2000) Fractionation of the REE during hydrothermal processes: constraints from the Bayan Obo Fe–REE–Nb deposit, Inner Mongolia, China. *Geochim Cosmochim Acta* 64(18):3141–3160. doi:10.1016/s0016-7037(00)00416-6
- Smith MP, Campbell LS, Kynicky J (2014) A review of the genesis of the world class Bayan Obo Fe–REE–Nb deposits, Inner Mongolia, China: multistage processes and outstanding questions. *Ore Geol Rev*. doi:10.1016/j.oregeorev.2014.03.007
- Soman A, Geisler T, Tomaschek F, Grange M, Berndt J (2010) Alteration of crystalline zircon solid solutions: a case study on zircon from an alkaline pegmatite from Zomba–Malosa, Malawi. *Contrib Mineral Petrol* 160(6):909–930. doi:10.1007/s00410-010-0514-2
- Spandler C, Hermann J, Rubatto D (2004) Exsolution of thortveitite, yttrialite, and xenotime during low-temperature recrystallization of zircon from New Caledonia, and their significance for trace element incorporation in zircon. *Am Mineral* 89(11–12):1795–1806

- Tao K, Yang Z, Zhang Z, Wang W (1998) Systematic geological investigation on carbonatite dykes in Bayan Obo, Inner Mongolia, China. *Scientia Geologica Sinica* 33:73–83
- Veksler IV, Dorfman AM, Dulski P, Kamenetsky VS, Danyushevsky LV, Jeffries T, Dingwell DB (2012) Partitioning of elements between silicate melt and immiscible fluoride, chloride, carbonate, phosphate and sulfate melts, with implications to the origin of natrocarbonatite. *Geochim Cosmochim Acta* 79:20–40. doi:10.1016/j.gca.2011.11.035
- Wall F, Niku-Paavola VN, Storey C, Muller A, Jeffries T (2008) Xenotime-(Y) from carbonatite dykes at Lofdal, Namibia: unusually low LREE:HREE ratio in carbonatite, and the first dating of xenotime overgrowths on zircon. *Can Mineral* 46:861–877. doi:10.3749/canmin.46.4.861
- Wang JW, Tatsumoto M, Li XB, Premo WR, Chao ECT (1994) A precise Th-232–Pb-208 chronology of fine-grained monazite—age of the Bayan Obo REE–Fe–Nb ore deposit, China. *Geochim Cosmochim Acta* 58(15):3155–3169. doi:10.1016/0016-7037(94)90043-4
- Wang KY, Fan HR, Xie YH, Li HM (2002) Zircon U–Pb dating of basement gneisses in the superlarge Bayan Obo REE–Fe–Nb deposit, Inner Mongolia. *Chin Sci Bull* 47(3):243–247. doi:10.1360/02tb9058
- Wang YX, Qiu YZ, Gao JY, Zhang QA (2003) Proterozoic anorogenic magmatic rocks and their constraints on mineralizations in the Bayan Obo deposit region, Inner Mongolia. *Sci China Ser D Earth Sci* 46:26–40
- Watson EB, Harrison TM (1983) Zircon saturation revisited—temperature and composition effects in a variety of crustal magma types. *Earth Planet Sci Lett* 64(2):295–304. doi:10.1016/0012-821x(83)90211-x
- Wiedenbeck M, Hanchar JM, Peck WH, Sylvester P, Valley J, Whitehouse M, Kronz A, Morishita Y, Nasdala L, Fiebig J, Franchi I, Girard JP, Greenwood RC, Hinton R, Kita N, Mason PRD, Norman M, Ogasawara M, Piccoli R, Rhede D, Satoh H, Schulz-Dobrick B, Skar O, Spicuzza MJ, Terada K, Tindle A, Togashi S, Vennemann T, Xie Q, Zheng YF (2004) Further characterisation of the 91500 zircon crystal. *Geostand Geoanal Res* 28(1):9–39. doi:10.1111/j.1751-908X.2004.tb01041.x
- Williams-Jones AE, Migdisov AA, Samson IM (2012) Hydrothermal mobilisation of the rare earth elements—a tale of “Ceria” and “Yttria”. *Elements* 8(5):355–360. doi:10.2113/gselements.8.5.355
- Woolley AR, Bailey DK (2012) The crucial role of lithospheric structure in the generation and release of carbonatites: geological evidence. *Mineral Mag* 76(2):259–270. doi:10.1180/minmag.2012.076.2.02
- Woolley AR, Kjarsgaard BA (2008) Carbonatite occurrences of the world: map and database. In: Geological survey of Canada, Open File, vol 5796. Geological Survey of Canada, pp 1 CD-ROM + 1 map
- Yang ZM, Woolley A (2006) Carbonatites in China: a review. *J Asian Earth Sci* 27(5):559–575. doi:10.1016/j.jseae.2005.06.009
- Yang ZM, Smith M, Henderson P, LeBas MJ, Tao KJ, Zhang PS (2001) Compositional variation of aeschynite-group minerals in the Bayan Obo Nb–REE–Fe ore deposit, Inner Mongolia, China. *Eur J Mineral* 13(6):1207–1214. doi:10.1127/0935-1221/2001/0013-1207
- Yang XM, Yang XY, Zheng YF, Le Bas MJ (2003) A rare earth element-rich carbonatite dyke at Bayan Obo, Inner Mongolia, North China. *Mineral Petrol* 78(1–2):93–110. doi:10.1007/s00710-002-0220-5
- Yang KF, Fan HR, Santosh M, Hu FF, Wang KY (2011a) Mesoproterozoic carbonatitic magmatism in the Bayan Obo deposit, Inner Mongolia, North China: constraints for the mechanism of super accumulation of rare earth elements. *Ore Geol Rev* 40(1):122–131. doi:10.1016/j.oregeorev.2011.05.008
- Yang KF, Fan HR, Santosh M, Hu FF, Wang KY (2011b) Mesoproterozoic mafic and carbonatitic dykes from the northern margin of the North China Craton: implications for the final breakup of Columbia supercontinent. *Tectonophysics* 498(1–4):1–10. doi:10.1016/j.tecto.2010.11.015
- Yuan ZX, Bai G, Wu CY, Zhang ZQ, Ye XJ (1992) Geological features and genesis of the Bayan Obo REE ore deposit, Inner-Mongolia, China. *Appl Geochem* 7(5):429–442
- Yuan ZX, Bai G, Zhang ZQ (2000) Trachytic rock and associated fenitization in the Bayan Obo ore deposit, Inner Mongolia, China: evidence for magmatic-hydrothermal mineralization related to a carbonatitic complex. *Acta Geol Sin* 74(2):148–153 (English edition)
- Yuan HL, Gao S, Dai MN, Zong CL, Gunther D, Fontaine GH, Liu XM, Diwu C (2008) Simultaneous determinations of U–Pb age, Hf isotopes and trace element compositions of zircon by excimer laser-ablation quadrupole and multiple-collector ICP-MS. *Chem Geol* 247(1–2):100–118. doi:10.1016/j.chemgeo.2007.10.003
- Zachariáš J, Wilkinson J (2007) ExLAM 2000: excel VBA application for processing of transient signals from laser ablation (LA-ICP-MS) of fluid inclusions and solid phases: ECROFI-XIX Biennial conference on European current research on fluid inclusions, Bern, Switzerland
- Zhang ZQ, Tang SH, Yuan ZX, Bai G, Wang JH (2001) The Sm–Nd and Rb–Sr isotopic systems of the dolomites in the Bayan Obo ore deposit, Inner Mongolia, China. *Acta Petrol Sin* 17(4):637–642
- Zhang PS, Tao KJ, Yang ZM, Yang XM, Song RK (2003) Rare earths, niobium and tantalum minerals in Bayan Obo ore deposit and discussion on their genesis. *J Rare Earths* 20(2):81–86